Determining the resolution limits of electron-beam lithography: direct measurement of the point-spread function

Vitor R. Manfrinato[a], Jianguo Wen[b], Lihua Zhang[c], Yujia Yang[a], Richard G. Hobbs[a], Bowen Baker[a], Dong Su[c], Dmitri Zakharov[c], Nestor J. Zaluzec[b], Dean J. Miller[b], Eric A. Stach[c], and Karl K. Berggren[a,*].

[a] Electrical Engineering and Computer Science Department, MIT

[b] Electron Microscopy Center, Argonne National Laboratory

[c] Center for Functional Nanomaterials, Brookhaven National Laboratory

* Corresponding author: berggren@mit.edu

Abstract:

One challenge existing since the invention of electron-beam lithography (EBL) is understanding the exposure mechanisms that limit the resolution of EBL. To overcome this challenge, we need to understand the spatial distribution of energy density deposited in the resist, that is, the point-spread function (PSF). During EBL exposure, the processes of electron scattering, phonon, photon, plasmon, and electron emission in the resist are combined, which complicates the analysis of the EBL PSF. Here, we show the measurement of delocalized energy transfer in EBL exposure by using chromatic aberration-corrected energy-filtered transmission electron microscopy (EFTEM) at the sub-10-nm scale. We have defined the role of spot size, electron scattering, secondary electrons, and volume plasmons in the lithographic PSF by performing EFTEM, momentum-resolved electron energy loss spectroscopy (EELS), sub-10-nm EBL, and Monte Carlo simulations. We expect that these results will enable alternative ways to improve the resolution limit of EBL. Furthermore, our approach to study the resolution limits of EBL may be applied to other lithographic techniques where electrons also play a key role in resist exposure, such as ion-beam-, x-ray-, and extreme-ultraviolet lithography.

Keywords: electron-beam lithography, point-spread function, electron energy loss spectroscopy, chromatic aberration, transmission electron microscopy, secondary electrons, volume plasmons, HSQ.

Electron-beam lithography (EBL) is the main top-down pattern-generation technique in nanotechnology and industry because it provides arbitrary patterning capabilities at the sub-5-nm scale.[1] EBL at this scale is increasingly important in templated self assembly of block-copolymers,[2-5] colloidal quantum dots,[6-8] nanowires,[9] and DNA origami.[10] Furthermore, the fabrication of novel plasmonic,[11] magnetic,[12] and nanoelectronic devices[13] would benefit from a complete understanding of the EBL exposure process. Since the invention of EBL 50 years ago,[14] the resolution-limiting factors of EBL have not been precisely quantified.[1, 15-19] To understand the resolution limits, we need to study each component of the EBL point-spread function (PSF),[19-22] which is a significant experimental challenge. The processes of electron scattering, phonon, photon, plasmon, and electron emission in the resist are combined, which complicates the understanding of the EBL PSF. Here, we disentangle the most important components involved in the EBL PSF at the sub-10-nm scale. We show direct evidence of the effect of electron scattering and delocalized processes on the EBL PSF by using recently developed chromatic-aberration-corrected energy-filtered transmission electron microscopy (EFTEM).[23] We further quantify the influence of volume plasmons (VPs) and secondary electrons (SEs) in EBL resolution by using momentum-resolved electron energy loss spectroscopy (EELS), sub-10-nm EBL, and numerical and Monte Carlo simulations. Understanding the factors contributing to the EBL PSF is critical to advance nanotechnology research and development. This understanding will help improve proximity effect correction algorithms[24-26] and push the resolution of EBL toward the sub-5-nm scale. The limiting factors in EBL may also limit other lithographic techniques, such as ion-beam and extreme-ultraviolet lithography.[27] In addition, the measurement of the EBL PSF at the ångström scale gives a unique measure of the interaction-volume of an electron beam with a sample, which is important for studying the resolution limits of scanning electron microscopy.[28, 29]

The PSF consists of the spatial distribution of energy density deposited in the resist and contains all physical phenomena that contribute to the resolution limit during the resist exposure. The measurement of the PSF enables the calculation of maximum pattern density or minimum pitch[19, 30, 31] and the estimation of the process latitude for a given resolution.[31, 32] We note that there are resolution-limiting factors that do not depend directly on the PSF, such as resist development,[18] feature collapse,[19] resist molecular structure, chemical diffusion (i.e., crosslinking redistribution), and chemical amplification processes. Previously, the PSF could be measured only lithographically by exposing single pixels (or other test structures) for a large dose range, followed by resist development.[20] One problem with this method is that the lithographic PSF contains many processes combined, leading to a challenging analysis. A direct measurement of each component of the PSF would be ideal to analyze and improve the resolution limits of EBL. During EBL, the electron beam can excite SEs, surface plasmons, VPs, phonons, and photons that may further deposit energy (or break bonds) in the resist. In Figure 1, we illustrate the two processes with the largest cross-sections, the generation of SEs and VPs. SEs have historically been considered to be the largest contributor to the EBL PSF.[20-22] The role of SEs on the PSF has been extensively modeled,[21, 22, 33-35] but it has not been directly measured to date. Previous results were limited by comparing the lithographic PSF to numerical models.[19, 31, 33] Furthermore, the role of VPs on SE emission has been studied[36-38], but the VP effect on the PSF has not been experimentally investigated.

In order to study the mechanisms that limit EBL resolution, we divided the lithographic PSF into three main components: (1) the direct-beam PSF; (2) the VP PSF; and (3) the SE PSF. The direct-beam PSF is the spatial distribution of local-energy-density deposited directly by the electron beam. We refer to energy deposition caused by SEs and VPs in the resist as delocalized exposure mechanisms. We consider these mechanisms as delocalized because these particles originate at an inelastic scattering position of the direct beam (to a good approximation), and then deposit energy away from the direct-beam PSF. Each PSF will have a characteristic broadening, which limits the resolution of EBL. We employed chromatic-aberration-corrected EFTEM to measure the direct-beam PSF. Furthermore, we observed that the excitation of VPs was the dominant (largest cross-section) energy loss mechanism. We performed EELS and Kramers-Krönig analysis[39] to obtain the VP PSF. The effect of SEs was simulated by numerical and Monte Carlo methods. We compared the direct-beam PSF, VP PSF, and simulated SE PSF to the lithographic PSF, determining the role of electron scattering, SEs, and VPs in the EBL PSF at the sub-10-nm scale.

We first measured the direct-beam PSF at 200 keV. The spherical- and chromatic-aberration-corrected EFTEM (Argonne chromatic aberration-corrected TEM – ACAT – C_C=1μm, C_S=2.5μm) is the ideal instrument for this measurement because the correction of chromatic aberration permits electrons with different energies to be imaged at the same focal plane. Figure 2 shows the direct-beam PSF measurement (see Supporting Information for details). We measured the number of electrons (ρ_{EFTEM}) that were transmitted through the resist as a function of radial position ($\vec{r}$) and energy loss (ε_f), as depicted in Figure 2a and shown in Figure 2c. In Figure 2d we show the direct-beam PSF, which was calculated using $\rho_{EFTEM}(|\vec{r}|; \varepsilon_f)$ for ε_f varying from 5 to 120 eV. The exit position of each electron is considered approximately equal to the position where this electron lost its energy. This approximation is reasonable because we achieved the single-inelastic-scattering regime and the effect of delocalization of inelastic scattering is small compared to the direct-beam PSF (see details in Supporting Information). The entire energy loss could be deposited locally (at $\vec{r}$) or a portion of this energy could be delocalized through the sample due to SE and VP propagation. The latter delocalization effects may lead to a broadening of the lithographic PSF relative to the direct-beam PSF and need to be analyzed.

The role of VPs on SE emission has been extensively investigated[36-38, 40, 41] in electron microscopy, but the effect of VPs on EBL resolution has not been established. VPs may decay via interband or intraband transitions, releasing a SE.[34, 36, 38] In the context of the free electron approximation, VPs with high momentum may decay and generate single electrons.[39, 42] We determined the dielectric function of our resist, hydrogen silsesquioxane (HSQ), to obtain the VP PSF. VPs may directly expose the resist or decay into SEs that expose the resist.

In Figure 3a-d we show the low-loss EELS spectrum and the Kramers-Krönig analysis[39] (KKA) used to determine the dielectric function of HSQ. The dielectric function provides the propagation decay length for an electromagnetic wave in HSQ. The decay length of VPs is considered to be the same as the decay length of an electromagnetic wave at the same energy, as previously detailed by references 43, 44. The VP decay length was then related to the VP PSF by the expression in the inset of Figure 3d. The rationale for this expression comes from considering the VP as a decaying cylindrical wave originating at the center of the electron beam. This functional form is similar to previous reports[43, 45, 46] (see Supporting Information for details). We did not consider VP scattering in this analytical form of the VP PSF. We compared the VP PSF with other PSFs in the next section.

To further investigate the VP peak, we performed EELS as a function of scattering angle or momentum (see Supporting Information for details on momentum-resolved EELS). In summary, the incident electron beam was tilted and the EELS spectrum was collected at specific angles (with 0.32 mrad angular resolution) defined by the collector aperture. In Figure 3e-f we show the evolution of the VP peak as a function of scattering angle. The VP dispersion in HSQ agreed with the expected behavior from the Lindhard model.[39] This result suggests that the energy loss peak at 22.5 eV in the EELS spectrum is indeed a VP resonance.

Furthermore, we performed atomistic simulation of the HSQ-cage structure (a significant portion of the exposed HSQ film still contains the HSQ-cage structure[47, 48]) to understand the small energy loss peaks or ‘shoulders’ at energies from 5 to 20 eV, as shown in Figure 3a. The electronic transitions from the simulation agree with the measured energy loss spectrum (see Supporting Information for details). The atomistic simulation result suggests that these peaks are vertical interband transitions, which are important decay pathways for VPs, which may produce SEs[36] that subsequently expose the resist.

In order to compare the effect of the SE PSF to the lithographic PSF, we performed numerical simulation of the SE PSF and Monte Carlo simulations of the lithographic PSF. The numerical SE PSF model presented here is sourced from References 22 and 33. This model is based on the classical inelastic scattering cross section for SE generation[21], modified-Bethe stopping power[29], and random walk approximation for SE propagation. This SE PSF model is simplified, but useful in giving an intuition of the role of SEs in EBL. The Monte Carlo modelling was carried out to achieve higher accuracy than the numerical method. The Monte-Carlo simulation is based on the Mott elastic cross section,[49] the classical inelastic cross sections[21], the modified-Bethe stopping power[29] (see Supporting Information for simulation details). The simulation results are presented in Figure 4 and it will be discussed in the next section.

Figure 4a describes the measurement of the lithographic PSF by the dot-exposure method (see Supporting Information for details),[20] which takes into account all physical phenomena relevant to EBL exposure (which were also described in Figure 1).

Figure 4b shows a comparison of the measured direct-beam PSF and VP PSF, and the two simulated SE PSFs, to the lithographic PSF. The largest contributor to the lithographic PSF at the sub-1-nm radius range was the direct-beam. This shows that despite SE emission and VP excitation, the spot size and electron scattering are the absolute limiting factors for fabrication of small, isolated features by EBL. The difference between the lithographic PSF and the direct-beam PSF is due to the sum of all delocalized processes in EBL exposure, including SEs and VPs. This result suggests that if a new resist could be developed to attenuate SE and VP emission, then the resulting lithographic PSF will be closer to the direct-beam PSF, therefore increasing the resolution.

Figure 4c shows the contribution of SEs and VPs to the lithographic PSF. (see calculation details in Supporting Information). We have compared the effects of SEs to VPs in the lithographic PSF by measuring the energy loss of each component by EELS. We assumed energy loss in the 10 to 50 eV range was due to VPs (VPs dominate the EELS spectrum in this range). We also assumed energy loss in the 50 to 1000 eV range was due to SEs. We did not consider cascade processes, such as inelastic scattering of SEs and VPs. The deposited energy density due to SEs was calculated by a convolution between the Monte-Carlo lithographic PSF and the instrument spot size. In the Monte-Carlo simulated PSF, the SEs dominate the spatial distribution of deposited energy density. The deposited energy density due to VPs was calculated by a convolution between the VP PSF and the direct-beam PSF for energies smaller than 50 eV. We normalized the deposited energy density due to SEs and VPs by their relative contribution to the total deposited energy (65% for SEs, 35% for VPs, determined by EELS).The total deposited energy density was the sum of the energy density deposited by SEs and VPs. The total deposited energy density obtained shows a satisfactory agreement with the lithographic PSF. The VPs were more important than SEs for a radius larger than 2 nm, limiting the fabrication of dense structures at the sub-10-nm scale (sub-10-nm pitch). Our simulations show that SEs do not have enough penetration depth to dominate the lithographic PSF in the 2 to 12 nm radius range. We limit the comparison between the energy density deposited due to VPs and SEs for radii smaller than the decay length of VP, that is, 12 nm. For radial distances larger than 12 nm, the VP PSF will further decrease by VP scattering, and the SE PSF will become the largest PSF component. This argument is consistent with previous comparisons of the lithographic PSF to simulations including SEs.[19, 31, 33]

We note that the PSF measurements obtained here were determined using a 10-nm-thick SiN_x membrane supporting the resist, and not a usual bulk substrate. Therefore, our experiments do not contain the contribution from backscattered electrons. In addition, our experiments were performed with electron beam energy of 200 keV, which is higher energy than in conventional EBL (≤ 125 keV). We simulated the lithographic PSF at 200 keV (including SEs but excluding VPs) considering a 20-nm-thick HSQ resist on top of 10-nm-thick SiN_x membrane and also on top of 300-μm-thick Si substrate (see simulation result on Supporting Information). The shape of the PSFs differ only for radii larger than 50 nm. There is also a similar experimental report confirming this trend for lower energies.[20] Therefore, the PSF measurements presented here are accurate for sub-50-nm radius. For further information on the effect of backscattered electrons in the PSF, we refer to References 25, 26, 50.

To conclude, We have shown for the first time the measurement of delocalized energy transfer in EBL exposure at the sub-10-nm scale by using chromatic aberration-corrected EFTEM. The measurements here focused at the EBL PSF at 200 keV and at the sub-10-nm length scale, without considering the effect of backscattered electrons. We have defined the role of spot size, electron scattering, SEs, and VPs in the lithographic PSF by performing electron microscopy and spectroscopy, sub-10-nm EBL, and numerical simulations. We expect that these results will enable novel ways to improve the resolution limit of EBL.

VPs can be excited by electrons and high-energy photons, such as extreme ultra violet (EUV).[51] EUV lithography is of increasing interest because it is considered the next generation lithographic technology for high volume manufacturing of semiconductors.[27, 52] Therefore, we note that the VP and SE PSFs may be important factors in the resolution limit analysis of EUV lithography. Furthermore, the experimental knowledge of the lithographic PSF at the sub-10-nm scale gives a unique way to measure electron-sample interaction volume, which is important to test theoretical models for scanning electron microscopy.[28, 34, 36, 38, 53]

Acknowledgements

We thank Jim Daley and Mark Mondol at the MIT Nanostructures Laboratory, and Yong Zhang at the MRSEC Shared Experimental Facilities at MIT for technical assistance. This material is based upon work supported as part of the Center for Excitonics, an Energy Frontier Research Center funded by the U.S. Department of Energy, Office of Science, Office of Basic Energy Sciences, under Award Number DE-SC0001088. The energy-filtered electron microscopy and momentum-resolved EELS were accomplished at the Electron Microscopy Center, Nanoscience and Technology Division of Argonne National Laboratory, a U.S. Department of Energy Office of Science Laboratory operated under Contract No. DE-AC02-06CH11357 by UChicago Argonne, LLC. The STEM lithography and EELS were carried out at the Center for Functional Nanomaterials, Brookhaven National Laboratory, which is supported by the U.S. Department of Energy, Office of Basic Energy Sciences, under Contract No DE-AC02-98CH10886. VRM, YY, and KKB would like to also acknowledge support from the Gordon and Betty Moore Foundation.

Supporting Information Available: Detailed description of experimental procedures, simulations, and analysis. This material is available free of charge via the Internet at http://pubs.acs.org

Conflict of Interest: The authors declare no competing financial interest.

References

1. Manfrinato, V.; Zhang, L.; Su, D.; Duan, H.; Hobbs, R.; Stach, E.; Berggren, K. *Nano Letters* 2013, 13, 1555-1558.
2. Ruiz, R.; Kang, H.; Detcheverry, F.; Dobisz, E.; Kercher, D.; Albrecht, T.; de Pablo, J.; Nealey, P. *Science* 2008, 321, 936-939.
3. Yang, J.; Jung, Y.; Chang, J.; Mickiewicz, R.; Alexander-Katz, A.; Ross, C.; Berggren, K. *Nature Nanotechnology* 2010, 5, 256-260.
4. Chang, J.-B.; Choi, H. K.; Hannon, A. F.; Alexander-Katz, A.; Ross, C. A.; Berggren, K. K. *Nature Communications* 2014, 5, 3305.
5. Hannon, A.; Ding, Y.; Bai, W.; Ross, C.; Alexander-Katz, A. *Nano Letters* 2014, 14, 318-325.
6. Cui, Y.; Bjork, M.; Liddle, J.; Sonnichsen, C.; Boussert, B.; Alivisatos, A. *Nano Letters* 2004, 4, 1093-1098.
7. Curto, A.; Volpe, G.; Taminiau, T.; Kreuzer, M.; Quidant, R.; van Hulst, N., *Science* 2010, 329, 930-933.
8. Manfrinato, V.; Wanger, D.; Strasfeld, D.; Han, H.; Marsili, F.; Arrieta, J.; Mentzel, T.; Bawendi, M.; Berggren, K. *Nanotechnology* 2013, 24, 125302.
9. Borgstrom, M.; Immink, G.; Ketelaars, B.; Algra, R.; Bakkers, E. *Nature Nanotechnology* 2007, 2, 541-544.
10. Kershner, R.; Bozano, L.; Micheel, C.; Hung, A.; Fornof, A.; Cha, J.; Rettner, C.; Bersani, M.; Frommer, J.; Rothemund, P.; Wallraff, G. *Nature Nanotechnology* 2009, 4, 557-561.
11. Ward, D.; Huser, F.; Pauly, F.; Cuevas, J.; Natelson, D. *Nature Nanotechnology* 2010, 5, 732-736.
12. Stipe, B.; Strand, T.; Poon, C.; Balamane, H.; Boone, T.; Katine, J.; Li, J.; Rawat, V.; Nemoto, H.; Hirotsune, A.; Hellwig, O.; Ruiz, R.; Dobisz, E.; Kercher, D.; Robertson, N.; Albrecht, T.; Terris, B. *Nature Photonics* 2010, 4, 484-488.
13. Leong, M.; Doris, B.; Kedzierski, J.; Rim, K.; Yang, M. *Science* 2004, 306, 2057-2060.
14. Wells, O.; Everhart, T.; Matta, R. *IEEE Transactions on Electron Devices* 1965, ED12, 556-563.
15. Broers, A.; Molzen, W.; Cuomo, J.; Wittels, N. *Applied Physics Letters* 1976, 29, 596-598.
16. Vieu, C.; Carcenac, F.; Pepin, A.; Chen, Y.; Mejias, M.; Lebib, A.; Manin-Ferlazzo, L.; Couraud, L.; Launois, H. *Applied Surface Science* 2000, 164, 111-117.
17. Cord, B.; Yang, J.; Duan, H.; Joy, D.; Klingfus, J.; Berggren, K. *Journal of Vacuum Science & Technology B* 2009, 27, 2616-2621.
18. Yang, J.; Cord, B.; Duan, H.; Berggren, K.; Klingfus, J.; Nam, S.; Kim, K.; Rooks, M. *Journal of Vacuum Science & Technology B* 2009, 27, 2622-2627.
19. Duan, H.; Manfrinato, V.; Yang, J.; Winston, D.; Cord, B.; Berggren, K. *Journal of Vacuum Science & Technology B* 2010, 28, C6H11-C6H17.
20. Rishton, S.; Kern, D. *Journal of Vacuum Science & Technology B* 1987, 5, 135-141.
21. Murata, K.; Kyser, D.; Ting, C. *Journal of Applied Physics* 1981, 52, 4396-4405.
22. Wu, B.; Neureuther, A. *Journal of Vacuum Science & Technology B* 2001, 19, 2508-2511.
23. Ercius, P.; Boese, M.; Duden, T.; Dahmen, U. *Microscopy and Microanalysis* 2012, 18, 676-683.
24. Chang, T. *Journal of Vacuum Science & Technology* 1975, 12, 1271-1275.

25. Babin, S.; Borisov, S.; Cheremukhin, E.; Grachev, E.; Korol, V.; Ocola, L.; Engelstad, R. *Emerging Lithographic Technologies Vii, Pts 1 and 2* 2003, 5037, 583-590.
26. Rommel, M.; Hoffmann, K.; Reindl, T.; Weis, J.; Unal, N.; Hofmann, U. *Microelectronic Engineering* 2012, 98, 202-205.
27. Gronheid, R.; Younkin, T.; Leeson, M.; Fonseca, C.; Hooge, J.; Nafus, K.; Biafore, J.; Smith, M.; LaFontaine, B.; Naulleau, P. *Proceedings SPIE* 2011, 7969.
28. Zhu, Y.; Inada, H.; Nakamura, K.; Wall, J. *Nature Materials* 2009, 8, 808-812.
29. Joy, D.; Luo, S. *Scanning* 1989, 11, 176-180.
30. Winston, D.; Manfrinato, V.; Nicaise, S.; Cheong, L.; Duan, H.; Ferranti, D.; Marshman, J.; McVey, S.; Stern, L.; Notte, J.; Berggren, K. *Nano Letters* 2011, 11, 4343-4347.
31. Manfrinato, V.; Cheong, L.; Duan, H.; Winston, D.; Smith, H.; Berggren, K. *Microelectronic Engineering* 2011, 88, 3070-3074.
32. Olkhovets, A.; Craighead, H. *Journal of Vacuum Science & Technology B* 1999, 17, 1366-1370.
33. Raghunathan, A.; Hartley, J. *Journal of Vacuum Science & Technology B* 2013, 31, 011605.
34. Luo, S.; Joy, D. *Scanning Microscopy* 1990, 127-146.
35. Kyser, D.; Viswanathan, N. *Journal of Vacuum Science & Technology* 1975, 12, 1305-1308.
36. Chung, M.; Everhart, T. *Physical Review B* 1977, 15, 4699-4715.
37. Ding, Z.; Shimizu, R. *Surface Science* 1989, 222, 313-331.
38. Kuhr, J.; Fitting, H. *Journal of Electron Spectroscopy and Related Phenomena* 1999, 105, 257-273.
39. Egerton, R. F., *Electron Energy-Loss Spectroscopy in the Electron Microscope*. Third ed.; Springer New York Dordrecht Heidelberg London: 1986.
40. Pijper, F.; Kruit, P. *Physical Review B* 1991, 44, 9192-9200.
41. Werner, W.; Salvat-Pujol, F.; Smekal, W.; Khalid, R.; Aumayr, F.; Stori, H.; Ruocco, A.; Stefani, G. *Applied Physics Letters* 2011, 99, 184102.
42. Maier, S. *Plasmonics: Fundamentals and Applications*. Springer, New York: 2007.
43. Ritchie, R.; Hamm, R.; Turner, J.; Wright, H.; Ashley, J.; Basbas, G. *Nuclear Tracks and Radiation Measurements* 1989, 16, 141-155.
44. Wolff, P. *Physical Review* 1953, 92, 18-23.
45. Hamm, R.; Turner, J.; Ritchie, R.; Wright, H. *Radiation Research* 1985, 104, S20-S26.
46. Udalagama, C.; Bettiol, A.; Watt, F. *Physical Review B* 2009, 80, 224107.
47. Choi, S.; Word, M.; Kumar, V.; Adesida, I. *Journal of Vacuum Science & Technology B* 2008, 26, 1654-1659.
48. Olynick, D.; Cord, B.; Schipotinin, A.; Ogletree, D.; Schuck, P. *Journal of Vacuum Science & Technology B* 2010, 28, 581-587.
49. Lowney, J. *Scanning* 1995, 17, 281-286.
50. Czaplewski, D.; Holt, M.; Ocola, L. *Nanotechnology* 2013, 24, 305302.
51. Raether, H. Excitation of Plasmons and Interband Transitions by Electrons. Springer Berlin Heidelberg: 1980; Vol. 88.
52. Brainard, R.; Hassanein, E.; Li, J.; Pathak, P.; Thiel, B.; Cerrina, F.; Moore, R.; Rodriguez, M.; Yakshinskiy, B.; Loginova, E.; Madey, T.; Matyi, R.; Malloy, M.; Rudack, A.; Naulleau, P.; Wuest, A.; Dean, K.; Henderson, C. *Proceedings of SPIE* 2008, 6923.
53. Joy, D. *Microbeam Analysis* 1995, 4, 125-129.

Captions

Figure 1. Illustration of electron scattering mechanisms in a resist during electron-beam lithography. (a) The electron travels through the resist and may exit the resist without a scattering event or it may experience an elastic scattering event, also without energy loss. We have defined the direct electron beam as the electron that passes through the sample. The elastic scattering event is depicted as a blue circle. (b) The electron beam may alternatively experience an inelastic scattering event. The energy loss in this event, depicted as a red circle, is transferred to a secondary electron that further deposits energy in the resist. (c) The electron may also suffer an inelastic scattering event and excite a VP. VPs are longitudinal oscillations of valence electrons taking place in the bulk of the resist. These VPs propagate and may directly expose the resist or decay as SEs, which further deposit energy in the resist. This VP decay process is depicted as a green circle. The hypothesis for the resist exposure is that a portion of the deposited energy density leads to molecular crosslinking or bond scission in the resist. The lithographic PSF is determined by a combination of all these energy-loss processes.

Figure 2. Measurement of the direct-beam PSF using chromatic-aberration-corrected energy-filtered TEM. (A) Schematic of the experiment. The focused incident electron beam had initial energy $\mathcal{E}_i$ of 200 keV and 0.8 nm full-width at half maximum. The electron beam is transmitted through the sample and may experience a radial deflection $\vec{r}$ and energy loss $\mathcal{E}$ due to scattering events. The electrons may be counted in EELS mode (ρ_{EELS}) or in EFTEM mode (ρ_{EFTEM}). Electrons were counted as a function of energy loss $\mathcal{E}$, $\rho_{\mathrm{EELS}}(\mathcal{E})$. Electrons were also counted as a function of radial distance $r = |\vec{r}|$ from the center of the beam for a filtered energy loss $\mathcal{E}_f$, $\rho_{\mathrm{EFTEM}}(r;\, \mathcal{E}_f)$. We used a 5 eV energy filter slit to select the energy loss $\mathcal{E}_f$ (see details in Supporting Information). (B) (squares) Total electron counts (ρ_{EFTEM} integrated over area A of 200

nm^2) as a function of energy loss $\mathcal{E}_f$ from 0 to 120 eV. The VP peak was observed at 22.5 eV. The integrated ρ_{EFTEM} (squares) correlates well with ρ_{EELS} (line). (C) $\rho_{EFTEM}(r; \mathcal{E}_f)$ with $\mathcal{E}_f$ from 5 to 120 eV. The shape of $\rho_{EFTEM}(r; \mathcal{E}_f)$ did not change significantly until the Si-L2,3 edges (core electrons) are excited at 99 eV. The inset shows a bright field EFTEM image used to compute $\rho_{EFTEM}(r; 20eV)$ (we considered ρ to be radially symmetric). (D) (dotted line) ρ_{EFTEM} in vacuum (no sample), $\rho_{EFTEM}^{vacuum}(r; 0eV)$; (dashed line) $\rho_{EFTEM}(r; 0eV)$; and (continuum line) radial distribution of deposited energy density, defined as 'direct-beam PSF' ($PSF_{(r)}^{direct-beam} = \sum_{\mathcal{E}_f=5eV}^{120\ eV} f(\mathcal{E}_f)\mathcal{E}_f \rho_{EFTEM}(r;\ \mathcal{E}_f)$, where $f(\mathcal{E}_f)$ is the fraction of electrons that lost energy $\mathcal{E}_f \pm 2.5$ eV– see details in Supporting Information). The direct-beam PSF represents the energy density locally deposited by the direct (or forward-scattered) electrons.

Figure 3. Measurement of the VP PSF and analysis of VPs. (a) (dashed line) EELS spectrum of 40-nm-thick HSQ on top of 10-nm-thick SiN_x at 200 keV. Kramers-Krönig analysis (KKA) provides a relationship between the EELS spectrum and the (continuum line) energy-loss function (proportional to the imaginary part of the reciprocal of the dielectric function - see details in Supporting Information). (b) Dielectric constant $E = \mathcal{E}_1 + i\mathcal{E}_2$ and complex index of refraction $\tilde{n} = n + ik$ from KKA. (c) Decay length $L = \frac{\lambda_0}{4\pi k}$ for an electromagnetic wave as a function of energy. (d) We calculated the VP PSF from the decay length at the VP energy, 22.5 eV. (e) VP energy as a function of scattering angle or momentum of the direct electron beam squared. We observed that VPs have a quadratic dispersion, as expected from the Lindhard model.[39] (f) EELS spectra with varying scattering angle. The increase of the VP-peak width for increasing scattering angle confirms the non-localized nature of the VPs.

Figure 4. Components of the Lithographic PSF. (a) Schematics of the dot-exposure method for measuring the lithographic PSF. (left) A single-pixel exposure generates an energy density profile

in a given plane of the resist (z=0), which is the lithographic PSF. The feature radius is defined when the deposited energy density is equal to the threshold energy density. We assumed constant threshold energy density and no chemical diffusion or crosslinking-redistribution effects. (right) Energy density contours at the threshold energy density and TEM micrographs of a developed feature, presented in top-view and side-view. We have repeated this process for many doses (units of Coulombs/pixel) and the lithographic PSF is constructed by plotting the reciprocal dose *versus* feature radius. (b) Components of the lithographic PSF (maximum value of all PSFs was set to unity): (blue) direct-beam PSF, (green) VP PSF, (purple) SE PSF by numerical method, (black circles) lithographic PSF by Monte-Carlo simulation including SEs, (gray) fitted lithographic PSF,[1] and (red squares - dataset 1 - and red triangles - dataset 2) lithographic PSF from dot-exposure method. From the direct-beam PSF to the lithographic PSF we have the total effect of delocalized energy transfer in EBL. The numerical SE PSF and Monte-Carlo lithographic PSF differ due to the simplified treatment of electron scattering in the numerical SE PSF model. (c) (blue) deposited energy density due to SEs, calculated from Monte-Carlo lithographic PSF including SEs and the instrument spot size; (black) deposited energy density due to VPs, calculated from VP PSF and direct-beam PSF for energies smaller than 50 eV; and (green) total deposited energy density (see calculation details in Supporting Information). The lithographic PSF was overlaid with the total deposited energy density. The VPs were necessary to match the total deposited energy density to the lithographic PSF.

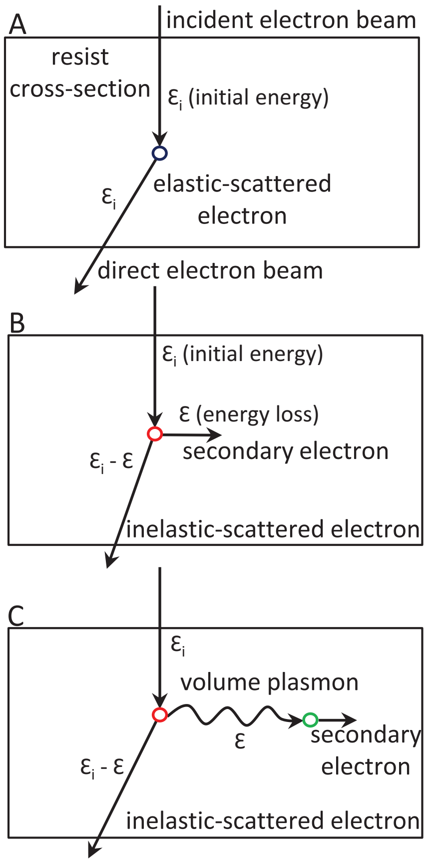
A
incident electron beam
resist
cross-section
ε_i (initial energy)
ε_i
elastic-scattered
electron
direct electron beam
B
ε_i (initial energy)
ε (energy loss)
secondary electron
$\varepsilon_i - \varepsilon$
inelastic-scattered electron
C
ε_i
volume plasmon
ε
secondary
electron
$\varepsilon_i - \varepsilon$
inelastic-scattered electron

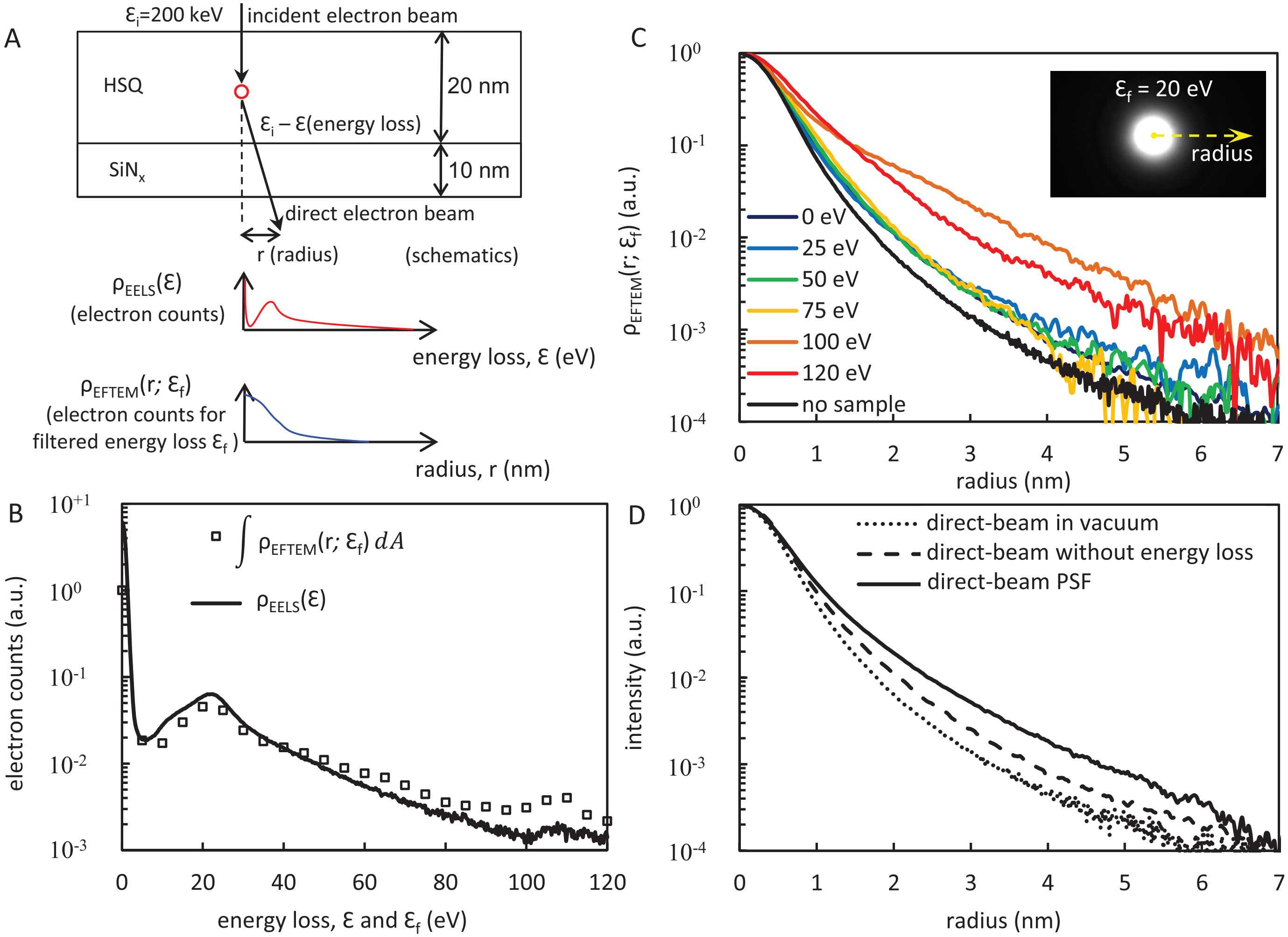A
Ɛi=200 keV
incident electron beam
HSQ
20 nm
Ɛi – Ɛ(energy loss)
SiNx
10 nm
direct electron beam
r (radius)
(schematics)
ρEELS(Ɛ)
(electron counts)
energy loss, Ɛ (eV)
ρEFTEM(r; Ɛf)
(electron counts for filtered energy loss Ɛf)
radius, r (nm)
B
10+1
100
10-1
10-2
10-3
electron counts (a.u.)
∫ ρEFTEM(r; Ɛf) dA
ρEELS(Ɛ)
0
20
40
60
80
100
120
energy loss, Ɛ and Ɛf (eV)
C
100
10-1
10-2
10-3
10-4
ρEFTEM(r; Ɛf) (a.u.)
Ɛf = 20 eV
radius
0 eV
25 eV
50 eV
75 eV
100 eV
120 eV
no sample
0
1
2
3
4
5
6
7
radius (nm)
D
100
10-1
10-2
10-3
10-4
intensity (a.u.)
direct-beam in vacuum
direct-beam without energy loss
direct-beam PSF
0
1
2
3
4
5
6
7
radius (nm)

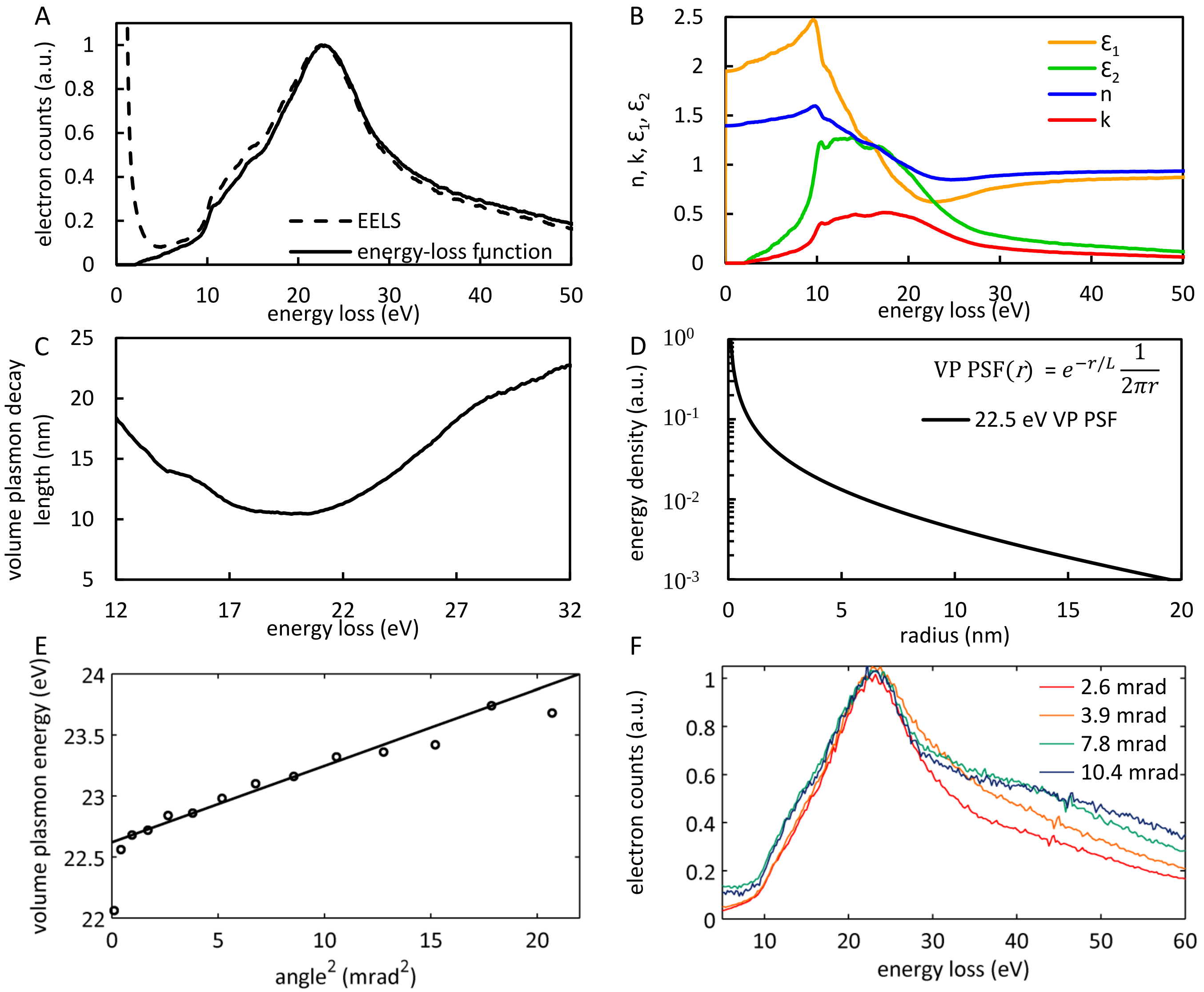
A
electron counts (a.u.)
energy loss (eV)
EELS
energy-loss function
B
n, k, ε1, ε2
energy loss (eV)
ε1
ε2
n
k
C
volume plasmon decay length (nm)
energy loss (eV)
D
energy density (a.u.)
radius (nm)
VP PSF(r) = e^{-r/L} 1/(2πr)
22.5 eV VP PSF
E
volume plasmon energy (eV)
angle² (mrad²)
F
electron counts (a.u.)
energy loss (eV)
2.6 mrad
3.9 mrad
7.8 mrad
10.4 mrad

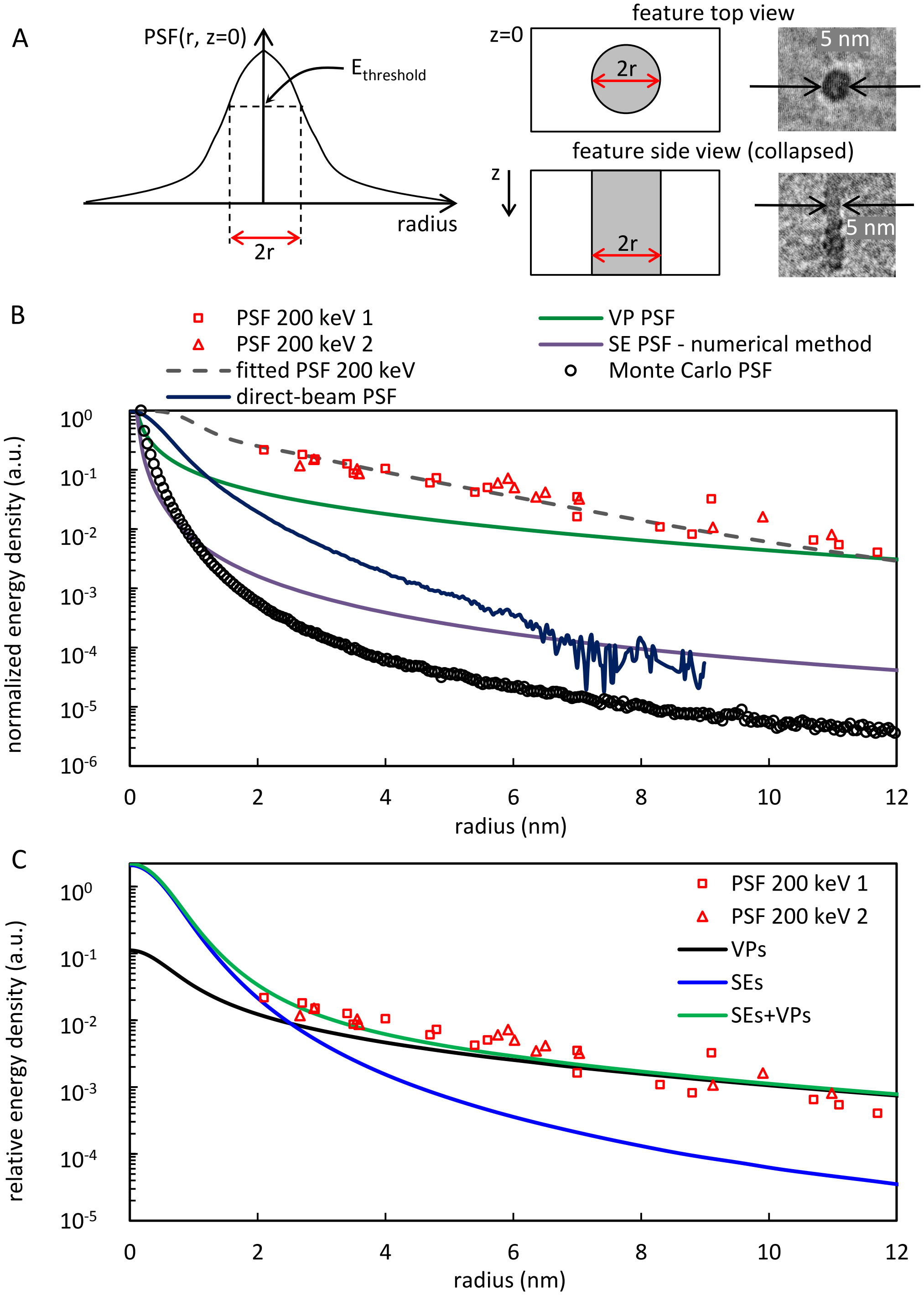
A
PSF(r, z=0)
E$_{threshold}$
radius
2r
feature top view
z=0
2r
5 nm
feature side view (collapsed)
z
2r
5 nm
B
PSF 200 keV 1
PSF 200 keV 2
fitted PSF 200 keV
direct-beam PSF
VP PSF
SE PSF - numerical method
Monte Carlo PSF
normalized energy density (a.u.)
10^{0}
10^{-1}
10^{-2}
10^{-3}
10^{-4}
10^{-5}
10^{-6}
0
2
4
6
8
10
12
radius (nm)
C
PSF 200 keV 1
PSF 200 keV 2
VPs
SEs
SEs+VPs
relative energy density (a.u.)
10^{0}
10^{-1}
10^{-2}
10^{-3}
10^{-4}
10^{-5}
0
2
4
6
8
10
12
radius (nm)

TOC

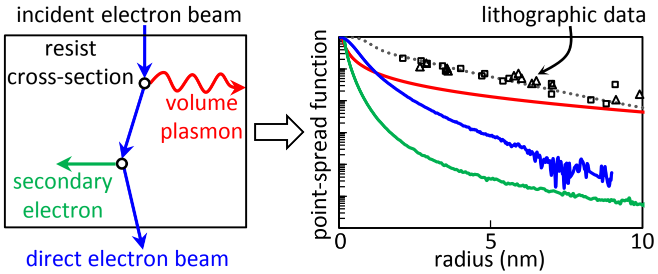
incident electron beam
resist
cross-section
volume
plasmon
secondary
electron
direct electron beam
lithographic data
point-spread function
0
5
10
radius (nm)

Supporting Information

Determining the resolution limits of electron-beam lithography: direct measurement of the point-spread function

Vitor R. Manfrinato[a], Jianguo Wen[b], Lihua Zhang[c], Yujia Yang[a], Richard G. Hobbs[a], Bowen Baker[a], Dong Su[c], Dmitri Zakharov[c], Nestor J. Zaluzec[b], Dean J. Miller[b], Eric A. Stach[c], and Karl K. Berggren[a,*].

[a] Electrical Engineering and Computer Science Department, MIT

[b] Electron Microscopy Center, Argonne National Laboratory

[c] Center for Functional Nanomaterials, Brookhaven National Laboratory

* Corresponding author: berggren@mit.edu

Table of Contents

1. Spherical- and chromatic-aberration corrected energy-filtered TEM

We performed energy-filtered transmission electron microscopy (EFTEM) on the sample described in Figure 2a (main text), consisting of a 20-nm-thick HSQ film on top of a 10-nm-thick SiN_x membrane.

EFTEM analysis operating at 200 keV with a FEI-TITAN, equipped with CEOS spherical- and chromatic-aberration correction (ACAT) was completed at Argonne National Laboratory. The chromatic aberration coefficient was 1 μm and the spherical aberration coefficient was 2.5 μm. We used a 50 μm diameter condenser aperture and focused the electron beam to a 0.8 nm FWHM spot, with a beam current of 230 pA. The sample was determined to be in focus by observing the phase-contrast and the Fast Fourier Transform of the image. In order to measure the electron-beam energy loss and maintain the incoming beam energy at 200 keV (as done in conventional electron-beam lithography (EBL)), we used the drift tube energy shift to set the spectrometer to a given energy and used a 5 eV energy slit for energy filtering. Due to the use of the drift tube, we considered data with energy loss less than 120 eV. Energy losses of more than 200 eV from the drift tube may affect the alignment of electron-optics. The spectrometer collection aperture used was 2 mm in diameter. We used a chromatic-aberration-corrected EFTEM to avoid chromatic aberrations in the objective lens. Therefore, the change of the transmitted electron spatial distribution as a function of energy loss was due to scattering in the sample, not due to the inability of the objective lens to properly focus these electrons on the conjugate image plane. The focal length of the incoming electron beam was not changed during the experiment, again to maintain the standard condition of EBL. The dwell time for image acquisition was varied from 0.1 to 1s to maximize the signal-to-noise ratio. The final EFTEM images were obtained by integrating over 40 frames and were aligned to each other using the built-in beam-drift alignment from Digital Microgaph (Gatan, Inc).

We imaged the transmitted electrons with EFTEM, i.e. the spatial distribution of electrons as a function of energy-loss. The measured transmitted electrons lost energy in the range from zero to 120 eV (±2.5 eV). Figure S1 shows the raw images of transmitted electrons as a function of energy-loss. Each image was taken in a nearby and fresh location of the sample. We observed negligible broadening of the electron-beam for energy-loss less than 90 eV. However, at 95 eV or higher energy-loss, a broader electron-beam was observed due to excitation of Si-L2,3 edges (core electrons).

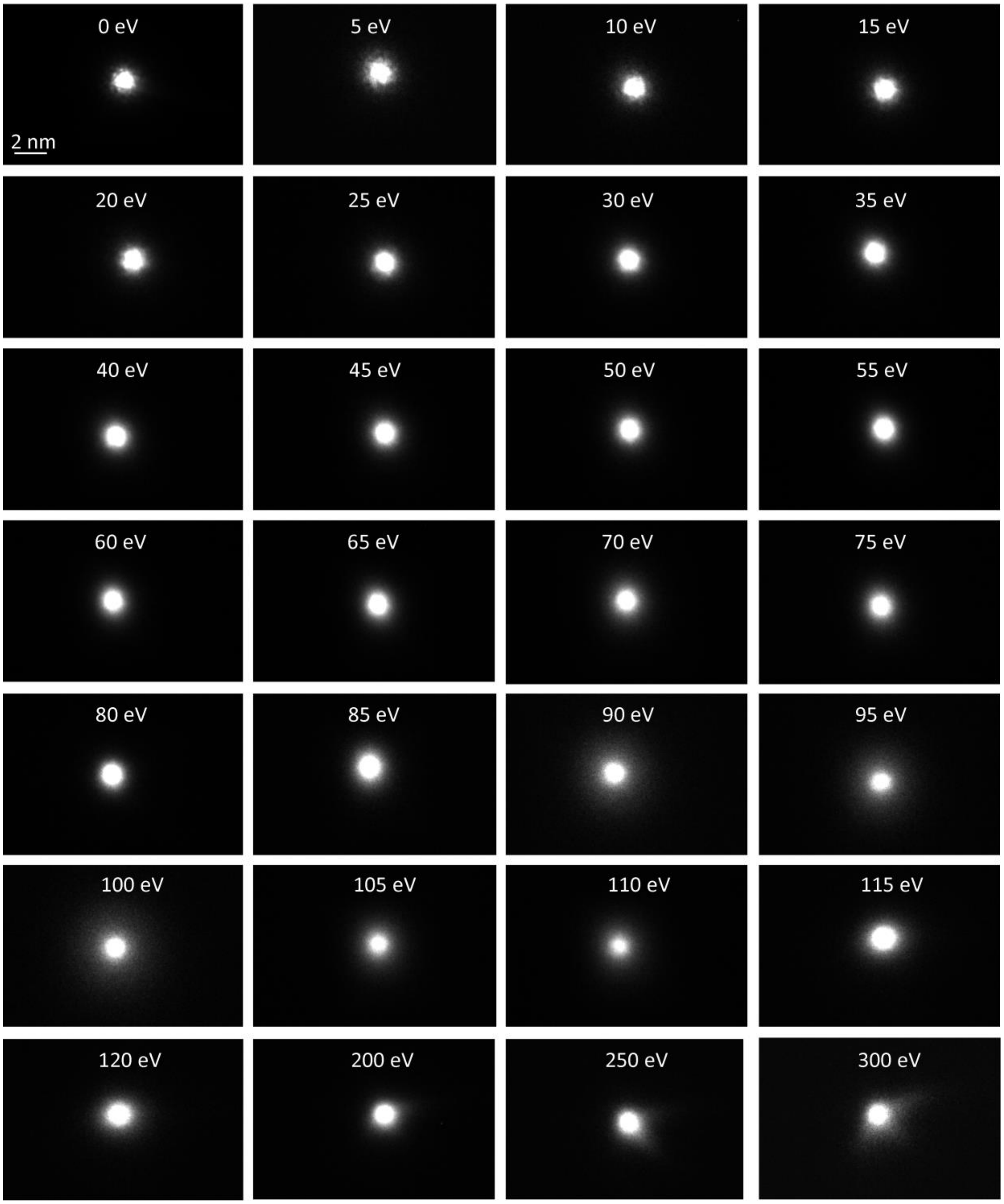

Figure S1. Energy-filtered images of transmitted electrons at 200 keV. The energy-loss ranges from 0 to 300 eV, with a 5 eV width. The dwell time was set to maximize the signal at each micrograph. The sample consists of 20-nm-thick HSQ on top of 10-nm-thick SiN_x. We observe a small spatial broadening of the transmitted electron distribution at

100 eV. For energies higher than 200 eV, we observe an asymmetric electron distribution, possibly due to high energy shift in the spectrometer.

To verify the physical integrity of the sample throughout the EFTEM measurements, we acquired EELS spectra as a function of time. If the electron beam induced sputtering of the sample, we would observe an attenuation of the volume plasmon (VP) peak with respect to the zero loss peak. Figure 2 shows that there was no significant variation in the VP peak intensity for up to 2.5 min of exposure, which is less than the dwell time used for each EFTEM image. We note that each EFTEM image was taken in a nearby and fresh location of the sample. We can observe a minimal decrease in the plasmon peak for exposures longer than 5 min. Consequently, electron-beam induced sputtering is not a critical issue for the image acquisition times used in this experiment.

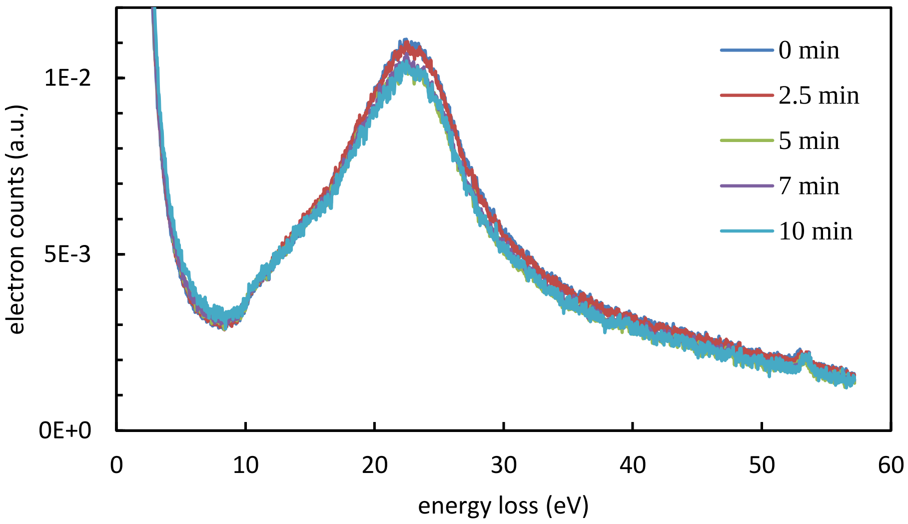

Figure S2. Low-loss electron energy-loss spectra for the HSQ/SiN$_x$ sample at different acquisition times, using a 0.8 nm FWHM spot size at 200 keV. For acquisitions longer than or equal to 5 min we observe a small decrease of the VP peak at 22.5 eV. This indicates minimal electron sputtering of the material.

2. Assumptions and calculation of the direct-beam point-spread function (PSF)

We have two main assumptions for measuring the direct-beam PSF:

(1) We consider that all energy lost by the direct-beam between 5 and 120 eV contributes to resist exposure.

(2) The position of the detected electron beam is approximately the position of the energy lost in the resist. For this consideration, we achieved single scattering regime and calculated that the delocalization of inelastic scattering is not significant compared to the direct-beam PSF.

To verify the appropriate range of energy loss to be taken into account in the direct-beam PSF measurement, we aquired an EELS spectrum from 0 to 700 eV on 20nm/10nm HSQ/SiN_x. We extrapolated the spectrum with a fitting curve up to 1 keV, as shown below. We considered 1 keV as a threshold energy because single inelastic scattering events with energies higher than 1 keV are likely to come from inner-shell ionization and generation of high-energy secondary electrons (SEs), which should not contribute significantly to the sub-10-nm direct-beam PSF. SEs with energies higher than 1 keV will not contribute significantly to the PSF at sub-10-nm radius because these SEs propagate hundreds of nanometers away from the point exposure, creating a uniform background of deposited energy at sub-10-nm radius.

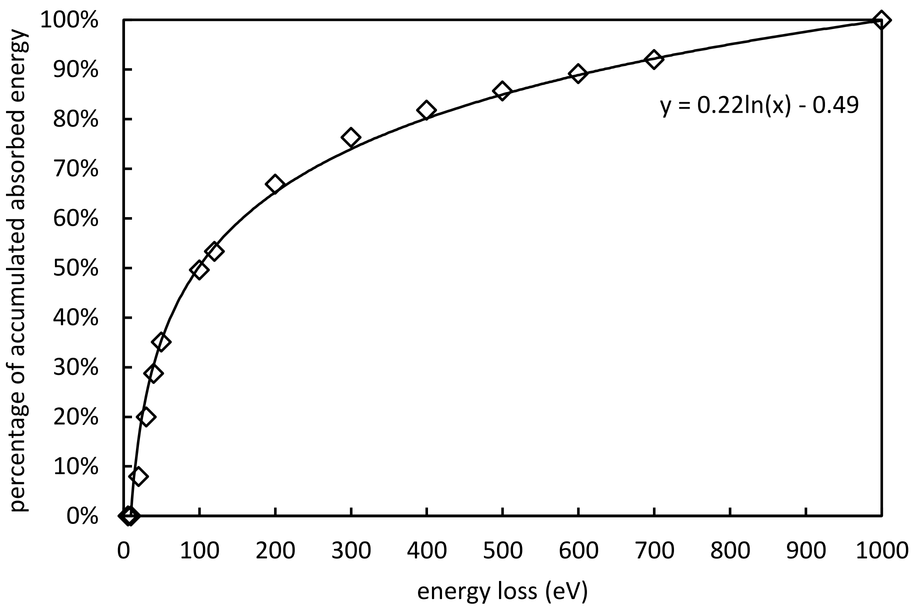

Figure S3. Plot of percentage of accumulted absorbed energy vs energy-loss in the range 10 to a given energy loss . We consider an energy threshold of 1 keV (which is equivalent to 100 %). 53% of the acumulated energy lost was in the 10 to 120 eV range. Single inelastic scattering events with energies higher than 1 keV are most likely to come from inner-shell ionization and generation of high-energy SEs, which should not contribute significantly to the sub-10-nm direct-beam PSF.

If we consider that all energy lost to the sample is due to electrons that lose 10 eV to 1 keV of energy, the 10 to 120 eV energy-loss range contains 53% of total absorbed energy. Therefore, the energy range from 10 to 120 eV captures the majority of the energy-loss of interest. In addition, VP resonance occurs between 10 and 50 eV, which contains 35% of the total absorbed energy. However, we note that the integrated tail of the VP peak extends up to ~100 eV. For example, a portion of the energy loss at 100 eV may be due to VP excitation.

Furthermore, we measured the energy-density threshold for HSQ exposure. We measured an average energy-loss per electron of 4.2 eV for a sample consisting of 20-nm-thick HSQ on top of 10-nm-thick SiN_x. We have estimated that HSQ absorbs 62% of the total energy-loss, and we considered a threshold dose for large area exposure of 230 electrons/nm^2. Therefore, we have estimated that the threshold energy density for HSQ exposure is ~30 eV/nm^3.

To evaluate our hypothesis of a single scattering regime in our HSQ+SiN$_x$ sample, we measured the log-ratio relation[1]:

$$\frac{t}{\lambda} = \log \frac{I_{total}}{I_{zero}} \tag{1}$$

where t is the sample thickness (HSQ+SiN$_x$), λ is the inelastic mean free path, I_{total} is the integrated EELS or summed EFTEM over all the spectrum, and I_{zero} is the integrated zero-loss peak of the EELS or the EFTEM zero loss peak. Single scattering regime requires t/λ <1.The t/λ measured was 0.26 using EFTEM and 0.24 using EELS (and 0.12 for SiN$_x$ only). Therefore, we may assume that the sample was in the single-scattering-event regime.

To evaluate whether inelastic scattering delocalization is critical to our analysis, we calculated the delocalization PSF based on an analytical formulation previously reported.[2] Figure S4 shows that the delocalization PSF decays by more than 4 orders of magnitude from 0.1 to 12 nm radius. The direct-beam PSF does not account for delocalization, but such effects would introduce a negligible broadening to the direct-beam PSF. Delocalization of inelastic scattering for energy loss larger than 25 eV is also negligible compared to the secondary-electron (as previously reported in electron-beam-induced deposition[3]) and volume-plasmon PSFs.

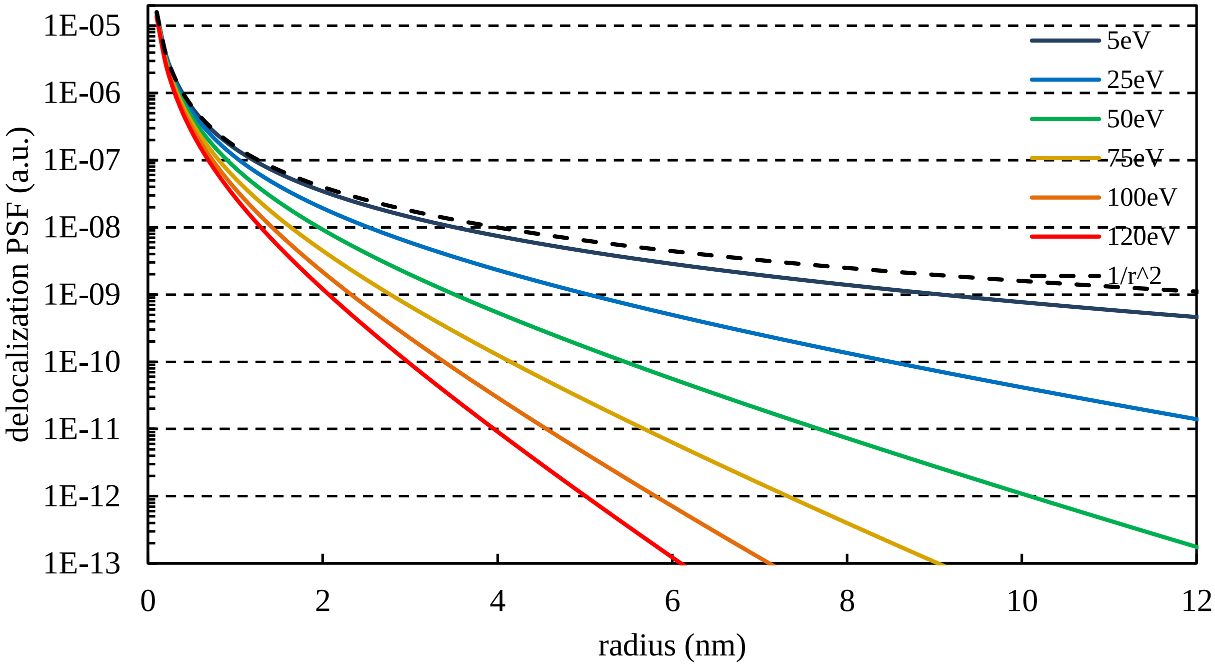

Figure S4. Radial distribution of the probability of energy loss (for 5, 25, 50, 75, 100, and 120 eV), that is, the inelastic or delocalization PSF.[2] The incident electron energy was 200 keV.

We have calculated the energy deposited by the electron beam, called 'direct-beam PSF', by weight averaging of the intensity of transmitted electrons from 2.5 to 122.5eV energy-loss (shown in Figure 4a of the main text):

$$PSF_{(r)}^{direct-beam} = \frac{\sum_{E=5\,eV}^{120\,eV} NE_{(E)} E \rho_{(r)}^{E}}{\sum_{E=5\,eV}^{120\,eV} NE_{(E)}} \left[\frac{eV}{nm^2}\right] \qquad (2)$$

where 'E' is the electron energy loss, $\rho_{(r)}^{E}$ is the spot size cross section at a given energy as a function of radial distance 'r', and $NE_{(E)}$ is the number of electrons.

3. EELS

Electron energy-loss spectroscopy (EELS) was performed on a Hitachi 2700C dedicated aberration-corrected STEM with a cold-field-emitter source (~ 0.4 eV energy spread) at 200 keV. A beam current of ~20 pA, 0.05 - 0.3eV/channel dispersion (depending on the desired energy range) and 2 mm collection aperture were used. The electron beam convergence semi-angle was 28 mrad, and the collection semi-angle was 14 mrad. The spectrum was taken with 0.04s dwell time with 10-50 frames.

The angle/momentum-resolved EELS was done on a FEI Tecnai F20ST TEM/STEM with a field-emitter-source (~1eV energy spread). An acceleration voltage of 200 kV, beam current of 60 pA, illuminated area 1.3 µm in diameter, 0.6 mm collection aperture, 970 mm camera focal length, 0.2eV/channel dispersion, were used. The dwell-time (0.1 to 100 s) and number of frames (1-100) were adjusted to maximize the signal-to-noise ratio without saturating the detector.

The relationship between the angle of an inelastic-scattered electron and the transferred momentum is[2]:

$$q^2 \cong {k_0}^2\left(\theta^2 + {\theta_E}^2\right) \tag{3}$$

where k_0 is 2505 nm^{-1} for 200 keV incident electrons, and θ_E is 0.065 mrad for 22.5 eV energy loss also with 200 keV incident electrons.

We calibrated the angular scale with a <111> oriented single-crystal silicon film. In the diffraction plane shown in Figure S5, we first aligned the [000] beam (non-diffracted) with the collection aperture. Then, we calibrated the beam tilt necessary to translate the [220] diffracted beam to the position of the [000] beam. The beam tilt was calibrated using an in-house computer script. Therefore, the tilt from [000] to [220] on Si corresponded to two times the Bragg scattering angle for the <220> direction, e.g. 13 mrad. EELS spectra were recorded only for specific values of scattering angle, from zero to 19.5 mrad with varying angular step size. The electron beam incident outside of the collection aperture was therefore blocked. The angular resolution was given by the collection angle or collection aperture size, corresponding to 0.32 mrad and 0.6 mm respectively. The convergence angle was also set to 0.32 mrad. The calibrated EELS system was then used to measure angle-resolved EELS for SiN$_x$, and HSQ.

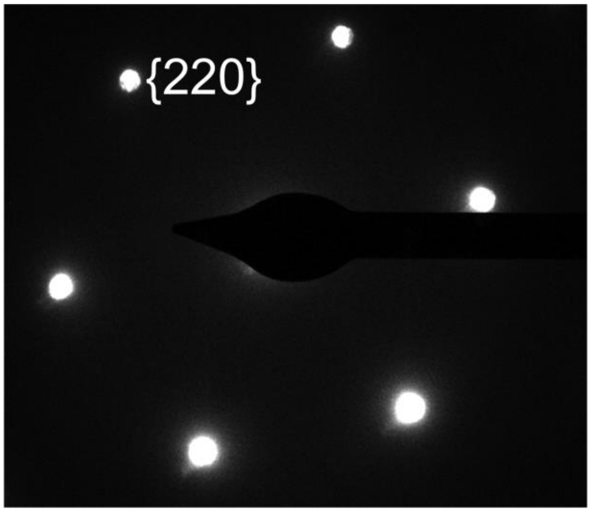

Figure S5. Electron diffraction of single-crystal Si oriented in the <111> direction. The <111> direction is into the plane of the page and is represented by the central spot, which was covered to enhance image-contrast. The six hexagonally arranged spots represent diffraction from the family of crystal planes[4] as shown.

The angle-resolved EELS spectrum of ~25 nm thick HSQ on top of 10-nm-thick SiN_x is shown in Figure S6 below. We observed from Figure S6, and Figure 3 in the main text, that the VP dispersion is subtle, shifting by 1.3 eV for a change in scattering angle of 0.0 to 4.5 mrad.

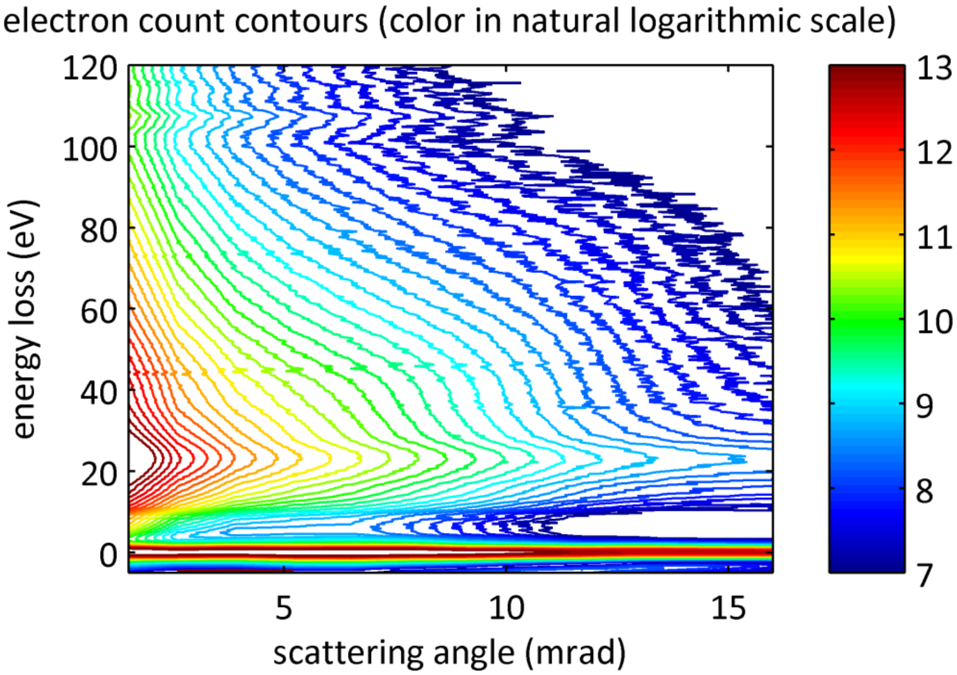

Figure S6. Momentum- or angle-resolved EELS. Electron count contours plotted as a function of electron energy-loss and scattering angle. The electron counts are shown in natural logarithmic scale. We observed the VP peak at 22.5 eV. We also observed a 'shoulder' that increases in intensity with increasing energy and line-width, which we call the dispersive VP component. See Figure 3e in the main text for the VP dispersion in HSQ.

The volume-plasmon peak usually presents a dispersive (leads to shift in energy) and a non-dispersive component. The non-dispersive component is due to a double scattering process, being an elastic scattering event with exchange of momentum plus a VP scattering event without exchange of momentum. In Figure S7 we plotted the ratio of volume-plasmon intensity to the zero-loss intensity. We observed that, above 5 mrad, the VP peak intensity correlated well with the zero-loss peak intensity. This suggests that the energy-loss spectrum above 5 mrad was dominated by the non-dispersive VPs. The observation of the dispersive VP peak in Figure 3e is expected because the maximum angle in Figure 3e is 4.5 mrad.

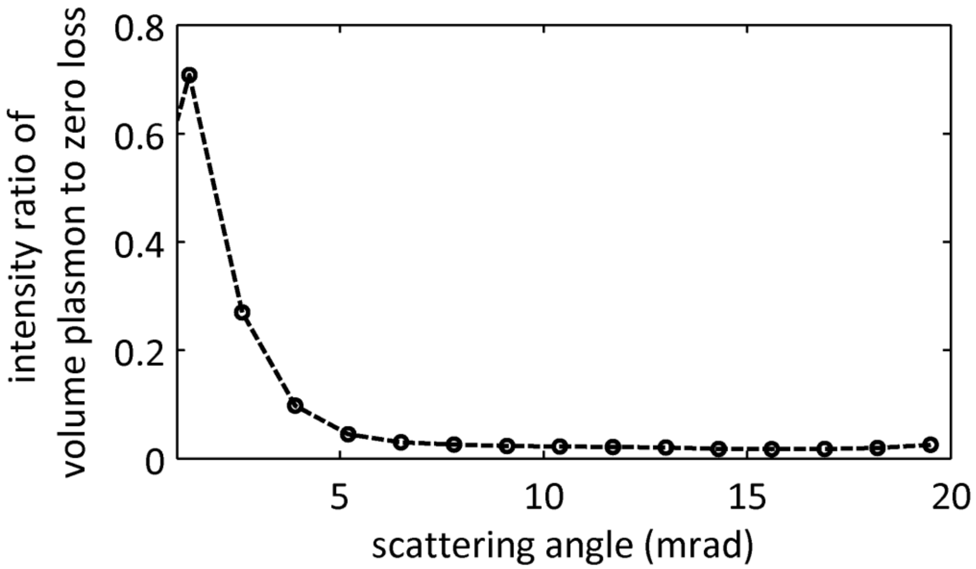

Figure S7. Ratio of the volume-plasmon intensity to the elastic (or zero loss) intensity as a function of scattering angle. We observed that the VP peak intensity correlated well with the elastic peak intensity for scattering angles larger than 5 mrad. This correlation suggests that the energy-loss spectrum is dominated by non-dispersive VPs for scattering angles larger than 5 mrad.

There are two factors to take into account in the EELS spectra shown in Figure 3e-f in the main text and in Figures S6 and S7: (1) the effect of SiN_x membrane; and (2) the effect of electron-beam damage.

We measured the t/λ ratio as discussed in the previous session to quantify the amount of energy-loss in 10-nm-thick SiN_x and ~25-nm-thick HSQ. For these experiments the collection aperture was 3 mm. We would like to perform measurements in a HSQ film that is thick enough to have the majority of the EELS signal from HSQ and not from SiN_x. We would also like to be in the single-scattering-event regime (t/λ <1). The log-ratio for 10-nm-thick SiN_x is $t/\lambda_{\mathrm{SiN}x} = 0.18$. While the log-ratio for ~30-nm-thick HSQ on top of 10-nm-thick SiN_x is $t/\lambda_{\mathrm{HSQ+SiN}x} = 0.40$. We estimated that 60% of energy-loss from the HSQ/SiN_x sample occurred in HSQ and that both samples were sufficiently thin to remain in the single-scattering-event regime.

To evaluate beam-damage, we noticed that the longest EELS acquisition time was 500 s (60 pA beam current), over a 1.3 µm diameter area, for 30 different scattering angles at the same position in the sample. We imaged the exposed area and monitored the VP peak before and after all acquisitions. We did not observe signs of sample damage (*e.g.* reduction of VP intensity).

4. Volume-Plasmon point-spread function: Kramers-Krönig Analysis (KKA)

The KKA method is discussed in details by Egerton in Reference 2. This method permits calculation of the dielectric function as a function of energy-loss. First we obtain the energy-loss function from the electron energy-loss spectrum in the single scattering regime:

$$J^1_{(E)} \approx S_{(E)} = \frac{I_0 t}{\pi a_0 m_0 v^2} Im\left[\frac{-1}{\varepsilon_{(E)}}\right] ln\left[1 + \left(\frac{\beta}{\theta_E}\right)^2\right] \tag{4}$$

J^1(E) is the electron energy-loss spectrum; *S*(E) is the electron energy-loss spectrum in the single scattering regime; I_0 is the intensity of the zero loss peak; *t* is the sample thickness; a_0 is the Bohr radius; m_0 is the electron rest mass; v is the incident electron velocity; $\mathcal{E}$(E) is the dielectric function; β is the collection semi-angle; θ_E is the characteristic scattering angle; and E is the energy loss.

The energy loss function, $Im\left[\frac{-1}{\varepsilon_{(E)}}\right]$, is related to the dielectric function $\varepsilon_{(E)}$. By using the KKA sum rule and KKA transformation, $\varepsilon_{(E)}$ is obtained. The complex index of refraction is then obtained by:

$$\boldsymbol{n} = n + ik = \sqrt{\boldsymbol{\varepsilon_{(E)}}} = \sqrt{\boldsymbol{\varepsilon_{1(E)}} + \boldsymbol{i\varepsilon_{2(E)}}} \tag{5}$$

We assumed that the VP decay length is the same as the decay length of an electromagnetic wave at the same frequency. A detailed discussion on the validity of this assumption can be found in References [5, 6]. The decay length L is the length scale where the intensity of the VP decays to 1/e of its original value:

$$L = \frac{\lambda_{0(E=22.5\ eV)}}{4\pi k_{(E=22.5\ eV)}} \tag{6}$$

where $\lambda_0$is the VP wavelength in vacuum, and k is the extinction coefficient or imaginary part of the complex index of refraction, both at the VP frequency.

Finally, the VP PSF is calculated using the relation:

$$PSF_{(r)}^{volume-plasmon} = \frac{e^{-r/L}}{2\pi r}\left[\frac{1}{nm^2}\right] \tag{7}$$

The factor 1/r is due to the cylindrical symmetry of the VP generation and propagation from a linear source perpendicular to the resist surface (the electron beam). This PSF form is similar to those used previously.[5, 7, 8]

5. Atomistic Simulation of HSQ Interband Transitions

Atomistic simulation of HSQ was performed with the *Abinit*[4, 9] package using projector augmented wave (PAW) density functional theory (DFT) under the local density approximation (LDA). To simulate a single HSQ cage molecule ($H_8Si_8O_{12}$) containing 28 atoms, the molecule was placed in a large vacuum box with dimension of $20 \times 20 \times 20$ Bohr^3. Different box sizes were tested and convergence was achieved for the chosen box size. The maximal plane-wave kinetic energy cutoff in the simulation was set to 50 Hartree. Convergence was also confirmed for this parameter value. Since the molecule-in-box model represents an isolated system, only one k point was included in the k-grid for the calculation.

5.1. Geometry Optimization

We first optimized the structure of the HSQ cage using Broyden-Fletcher-Goldfarb-Shanno minimization. The HSQ cage structures before and after optimization are illustrated in Figure S8. Simulated structural parameters are compared to experimental values obtained from XRD[10] in Table S1, confirming that the simulation generates correct HSQ cage structure.

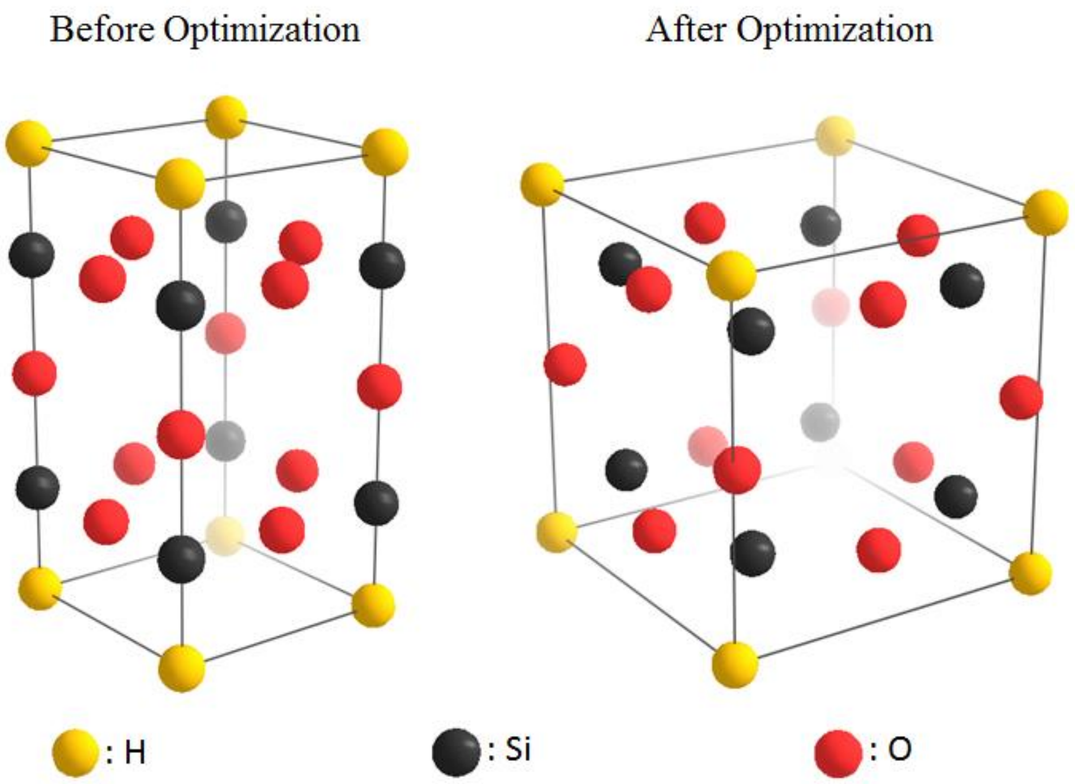

Figure S8. Cage structures of a single molecule of HSQ before and after structural optimization. We note that HSQ is an amorphous material that contains cage and network structures.

	Experiment[10]	Simulation
bond length $R_{Si\text{-}O}$	162 pm	173 pm
bond angle $A_{Si\text{-}O\text{-}Si}$	147.5°	144.5°
bond angle $A_{O\text{-}Si\text{-}O}$	109.6°	108.5°

Table S1. Comparison of structural parameters obtained from experiment[10] and simulation.

5.2. Electronic Structure

We then calculated the electronic structure of a HSQ cage using DFT. Goedecker-Teter-Hutter LDA pseudopotentials[11] were used for H, Si, and O atoms. Only the valence electrons were considered under the frozen-core approximation. Figure S9 illustrates the calculated density of states (DOS) for a HSQ cage.

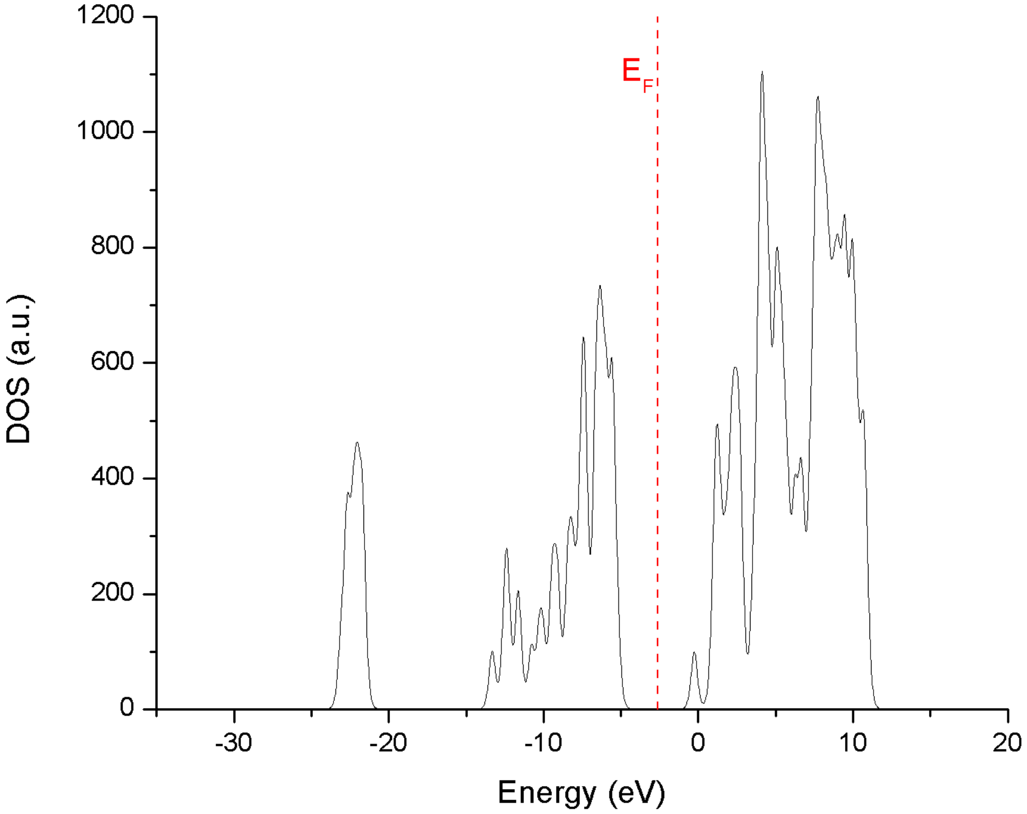

Figure S9. Simulated density-of-states (DOS) for a HSQ cage. The δ function representing each molecular orbital is smeared by an energy of 0.01 Hartree. The Fermi level is indicated by the red dashed line.

5.3. Optical Properties

Simulation of HSQ optical properties is based on the simulation result of its electronic structure. Random phase approximation (RPA) was used to calculate the dielectric function ϵ of HSQ. The energy-loss function was thus calculated from $Im(-1/\epsilon)$. The energy-loss function is shown in Figure S10. By comparing the simulated energy-loss function with experimentally obtained EELS data, we conclude that the VP resonance is either not resolved or strongly underestimated by the simple DFT-LDA calculation of an isolated HSQ cage molecule. However, interband transitions are resolved and lead to peaks in the simulated energy-loss function. In the experiment, the energy-loss is dominated by VP resonance. So, to better compare the simulation with the experiment and determine the contribution from interband transitions, we performed a second-derivative on the EELS spectrum to find the interband transitions. Table 2 shows the comparison between EELS interband transitions with the simulated interband transitions. For proper comparison, we shifted the simulated peaks by +2.46 eV. It can be seen that simulation and experiment achieve a reasonable agreement. It was necessary to shift the simulated peaks because the DFT-LDA method is known to underestimate the band-gap, or energy intervals between molecular orbitals.

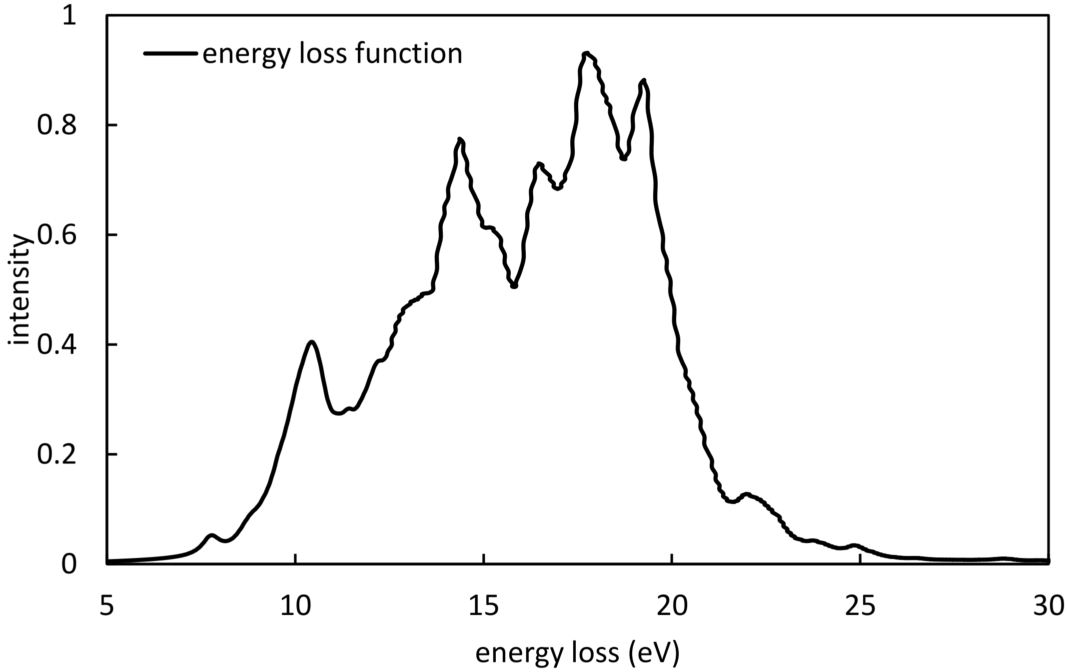

Figure S10. Simulated energy-loss function of an isolated HSQ cage molecule.

measured peaks (eV)	6.3	7	8.5	10.5	12.1	12.9	14.4	-	-	17.3	18.5	19.8	21	22.5
simulated peaks (eV)	-	7.8	-	10.5	12.2	13	14.4	15.1	16.4	17.6	-	19.3	-	22

Table S2. Comparison between measured peaks in the low-loss EELS spectrum with atomistic simulation of interband transitions of HSQ-cage structure.

6. Simulation of the secondary-electron point-spread function

The SE PSF model presented here is inspired by works of Hartley[12] and Neureuther[13] and is illustrated in Figure S11. The model presented here is simplified but effective in giving an intuition of the role of SEs in EBL.

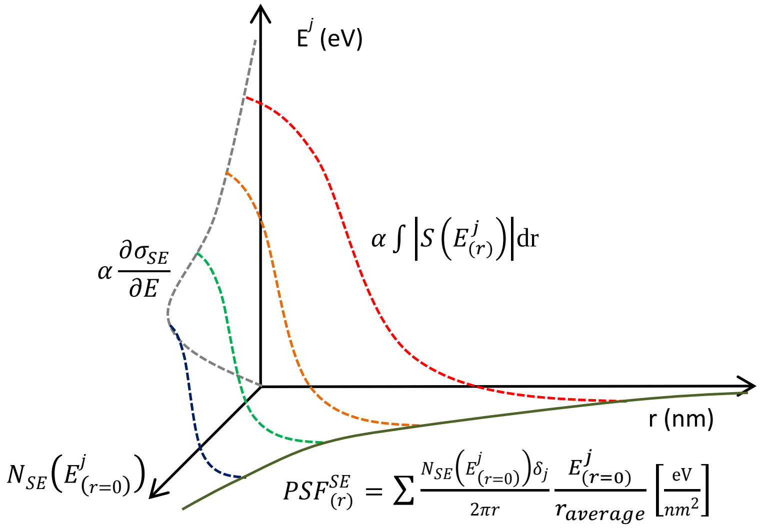

Figure S11. Illustration of the secondary-electron (SE) PSF model. Number of SEs N_{SE} *versus* SE energy E^j *versus* radial distance *r*. The number of SEs as function of energy is given by the differential cross-section $\frac{\partial \sigma_{SE}}{\partial E}$. From the position r=0, the SEs travel away from the center losing energy continuously. The colored lines represent the energy of SEs at different initial energies at *r*=0. High-energy SEs propagate longer distances but are in smaller number. The rate of energy loss is given by the modified Bethe stopping power. To estimate the electron penetration depth from the maximum penetration depth, we use the random-walk approximation $r_{average} = \frac{r_{max}}{\sqrt{N}}$, where N is the number of inelastic collisions. The $PSF^{SE}_{(r)}$.is obtained by the summation of the energy loss density of all electrons at a given radius.

SE Generation: The number of secondary electrons generated at radial distance ‘ *r=0*’with energy $E^{j}_{(r=0)}$ is given by:

$$N_{SE}\left(E^{j}_{(r=0)}\right) = \frac{\partial \sigma_{SE}}{\partial E} n_E N_{pe} l \, \left[\frac{\# e^-}{erg}\right] \tag{8}$$

$E^{j}_{(r)}$ is the SE energy as a function of radial distance r, starting with energy j at $r = 0$. $\frac{\partial \sigma_{SE}}{\partial E}$ is the classical differential electron inelastic cross section (probability of SE emission per unit energy) for core and valence electrons, n_E is the electron density, N_{pe} is the number of incident primary electrons, and l is the resist thickness.

SE propagation: The maximum propagation and random-walk (based on spherical cross section) estimation of SE propagation is given by:

$$r_{max} \approx \frac{E^{j}_{(r=0)}}{\left|S\left(E^{j}_{(r=0)}\right)\right|} \tag{9}$$

$$r^{j}_{average} = \frac{r_{max}}{\sqrt{N}} \tag{10}$$

where $\left|S\left(E^{j}_{(r-\Delta r)}\right)\right|$ is the stopping power for low-energy electrons, and N is number of inelastic collisions

SE energy deposition: The linear-density of deposited energy along the averaged (random walk) secondary-electron path is given by:

$$\frac{\Delta E^{j}_{(r)}}{\Delta r_{average}} = \frac{E^{j}_{(r=0)}}{r^{j}_{average}} \, \left[\frac{erg}{nm}\right] \tag{11}$$

SE point-spread function (SE PSF): The final calculated SE PSF is given by:

$$PSF^{SE}_{(r)} = \sum_{j=10\ eV}^{Eprimary/2} \frac{N_{SE}\left(E^{j}_{(r=0)}\right)\Delta E_j}{2\pi r} \frac{E^{j}_{(r=0)}}{r^{j}_{average}} \delta_{j>\left|S\left(E^{j}_{(r=0)}\right)\right| r^{j}_{average}} \, \left[\frac{\mathrm{erg}}{nm^2}\right] \tag{12}$$

The term $\delta_{j>\left|S\left(E^{j}_{(r=0)}\right)\right| r^{j}_{average}}$ (=1 if the inequality is satisfied) removes electrons that will not reach a distance $r^{j}_{average}$ from the sum. The term ΔE_j is the energy increment of the sum (1 eV in the simulation in this work).

7. Monte Carlo simulation of the lithographic point-spread function

Our goal is to have a trustworthy Monte-Carlo model to simulate the lithographic PSF and compare with experimental results. The physics of our Monte Carlo code, mainly based on references 14, 15, is summarized below.

7.1. Stopping power: We used Joy's Bethe-modified stopping power[16], which is accurate with respect to experimental data from 50 eV to 30 keV, and is a reasonable approximation from 10 eV to 30 keV.[17] We used the relativistic Bethe stopping power for electrons with energies higher than 30 keV.

7.2. Elastic cross section: We used the Mott elastic cross-section, which is known to be more accurate than Rutherford at lower energies (<10 keV).[18]

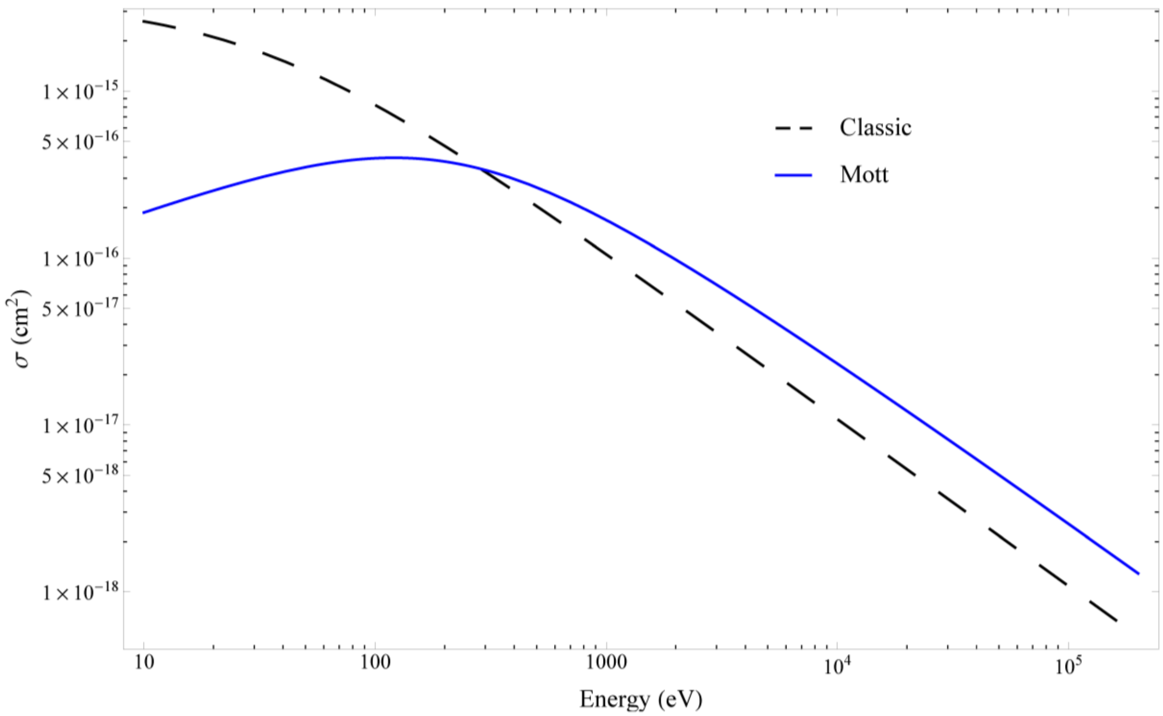

Figure S12. Elastic electron cross-section as a function of incident electron energy. The Mott cross section provides higher accuracy for lower primary electron energies than does the screened Rutherford cross-section.

7.3. Inelastic cross section: In Figure S13 we compared the following inelastic cross sections: (1) Classic;[14](2) Moller (as used in *Casino*[18]); (3) Moller for valence electrons and Gryzinski[19] for core electrons; and (4) Moller for valence electrons and Vriens for core electrons,[12, 13] named "Moller+Vriens". The lower bound cut off energy for inelastic scattered electrons was 10 eV.

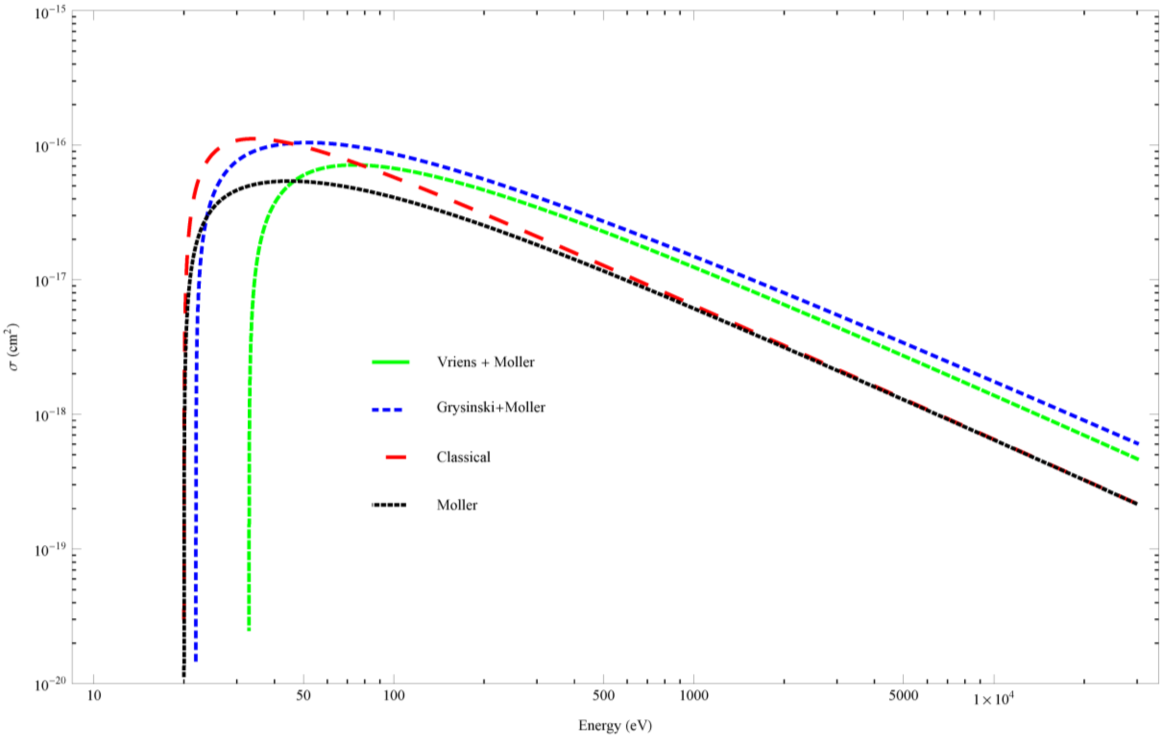

Figure S13. Inelastic electron cross-section as a function of incident electron energy. The Moller model gives the smallest cross-section while Grysinski model gives the largest cross-section for large energies.

We chose to simulate the SEs in the main text using the classical inelastic cross section because this model fits well with the lithographic PSF from ~10 to ~1000 nm.[20-22] We also tested the Moller+Vriens model, which provides a higher inelastic cross-section causing the SEs to have a larger effect on the PSF. As shown in Figure S14, the PSF using the Moller+Vriens model is wider than the PSF with the classic model.

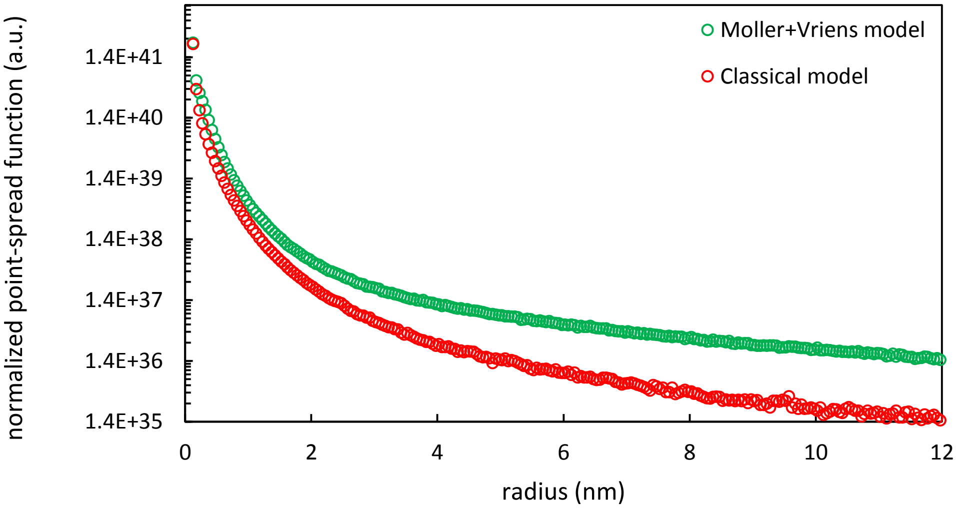

Figure S14. Monte-Carlo-simulated PSFs with different inelastic electron cross-sections. Red circle is the PSF using the classical inelastic cross section, green circle is the PSF with the Moller+Vriens inelastic cross section.

To evaluate whether SEs originated from direct atomic ionization (valence and core electrons) and not VPs (and not SEs generated from VPs) could be responsible for the lithographic PSF, we compared the lithographic PSF to two different Monte-Carlo simulated PSFs. Here, we included the effect of the instrument spot size (shown in Figure 2 of the main text). Figure S15 shows that the classical and the Moller+Vriens inelastic scattering models did not generate PSFs that match the shape of the lithographic PSF. This result suggests that SEs are not sufficient to simulate the lithographic PSF at the sub-12-nm scale. As is discussed in the main text and detailed in the next section, the total deposited energy density including SEs and VPs shown in Figure 4c better represents the lithographic PSF.

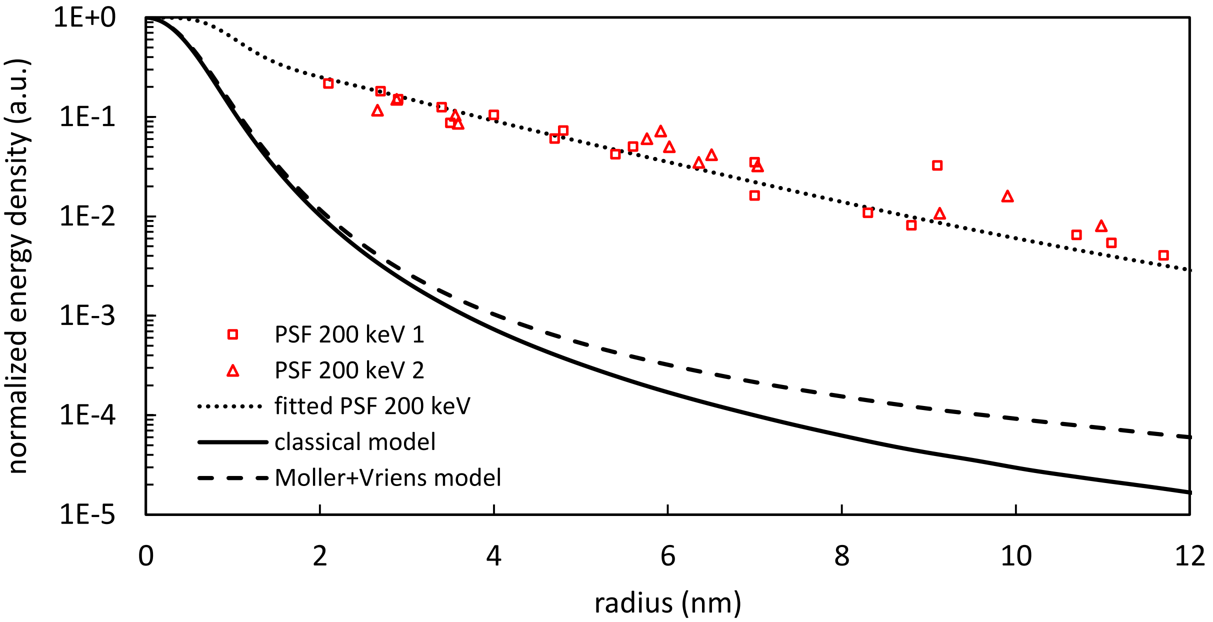

Figure S15. Comparison between the lithographic PSF and Monte-Carlo simulated PSFs convolved with the instrument spot size (maximum value of all PSFs was set to unity): (red squares represent dataset 1 and red triangles represent dataset 2) lithographic PSF from dot-exposure method; (dotted line) fitted lithographic PSF previously reported,[23] which is accurate down to 1 nm radius because this fitted PSF was obtained using 2-nm-wide feature as test structure; (continuum line) Monte-Carlo simulated PSF including SE generation using the classical inelastic cross section model; (dashed line) Monte-Carlo simulated PSF including SE generation using the 'Moller+Vriens' inelastic cross section model. We used the elastic cross section and stopping power models described in section 7.1 and 7.2.

In addition, we compared the Monte Carlo PSF with the numerical SE PSF (both simulations do not include VPs). Figure 4b in the main text shows a significant disagreement between these two models. Figure S16 below shows only a similar trend between these two PSFs from 10 to 100 nm radius. The numerical SE PSF is simplified and it does not take into account the complex scattering by the direct-beam and SEs. Therefore, we rely on the Monte Carlo simulation for analyzing the role of SEs in the lithographic PSF.

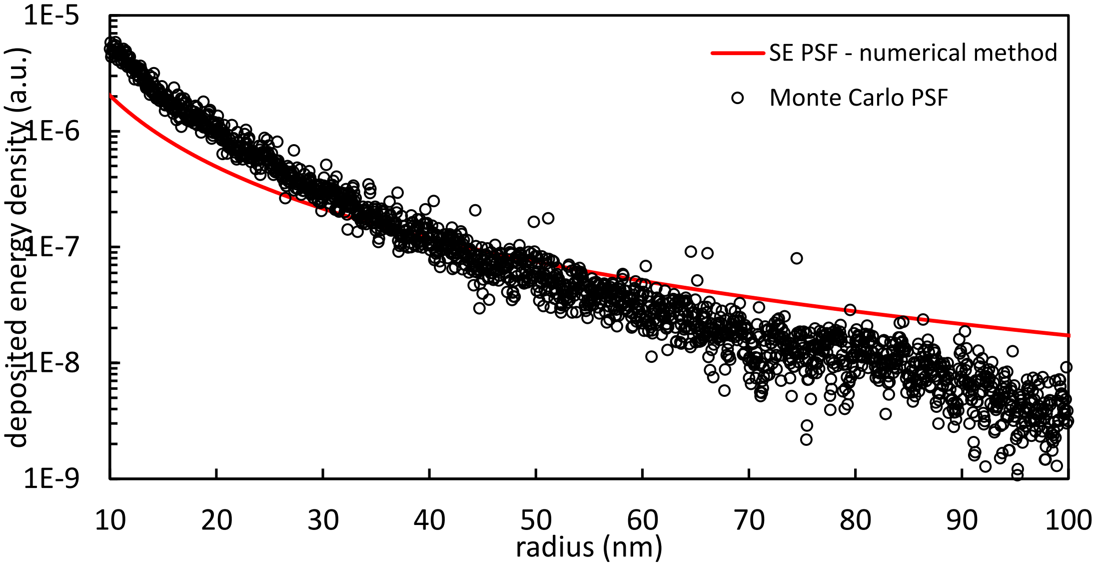

Figure S16. Comparison between the numerical SE PSF, described in the previous section, to the Monte-Carlo PSF. Both PSFs were calculated using the classical inelastic scattering cross section and the modified Bethe stopping power for electron energies smaller than 30 keV.

To understand the effect of backscattered electrons in the PSF, we simulated two PSFs, one with the 10-nm-thick SiN$_x$ supporting membrane (which should not show the effect of backscattered electrons) used throughout this work, and a more traditional 300-µm-thick Si substrate. As shown in Figure S17, the effect of backscattered electrons is apparent for radius larger than 50 nm. Therefore, the PSF measurements presented in the main text are valid for sub-50-nm radius, which can be useful to estimate the resolution limit of dense structures with sub-50×50nm^2 area.

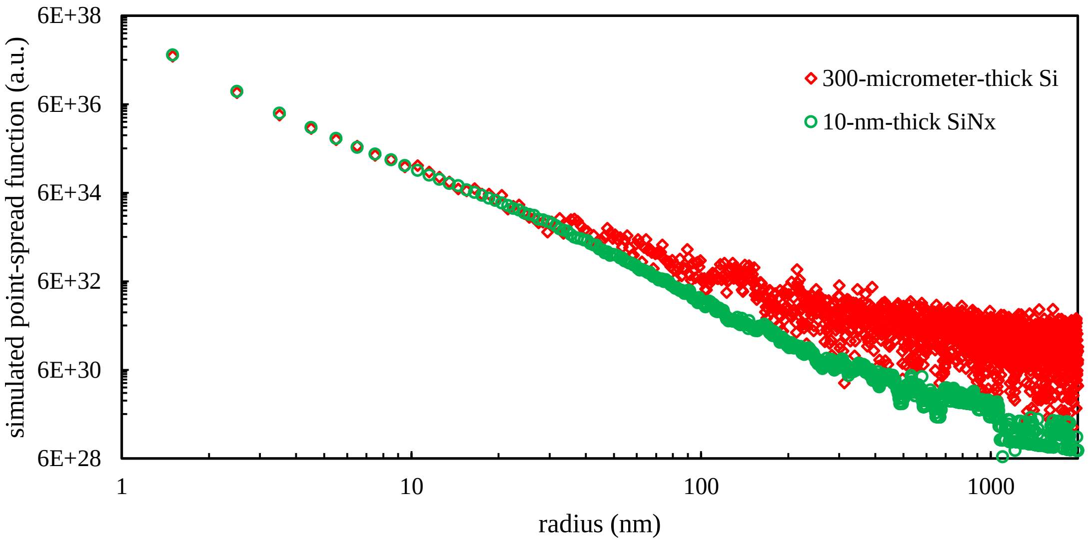

Figure S17. Monte-Carlo simulated PSFs with different supporting substrates. These simulations include SE generation but do not include VP generation. (green circle) Monte-Carlo PSF of 20-nm-thick HSQ on top of 10-nm-thick SiN_x membrane. (red diamond) Monte-Carlo PSF of 20-nm-thick HSQ on top of 300-µm-thick Si substrate. We used the classical inelastic scattering model for both PSFs. The other models used were previously described in this section. We observed a deviation between the PSFs for radius larger than 50 nm.

8. Lithographic point-spread function

8.1. Sample processing

Samples were prepared by spin-coating HSQ (1% solids XR-1541, Dow Corning) on 10-nm-thick SiN_x membranes (TEMwindows.com) at a spin-speed of 8 krpm. The resulting HSQ thickness was 10 nm. To avoid thermally-induced cross-linking of HSQ, which might lead to a loss in resolution, no pre-exposure bake was performed[24]. After exposure, samples were immersed in a salty developer (1% weight NaOH + 4% weight NaCl)[24] for 4 min at 24°C, rinsed under deionized water for 2 min, rinsed in isopropyl alcohol for 10 s, and gently blown dry with nitrogen gas for 1 minute. The typical total processing period from spin coating to development was about 4-5 days.

8.2. STEM lithography

Exposures were performed on a Hitachi HD 2700C dedicated aberration-corrected scanning transmission electron microscope (STEM) with a cold-field-emitter source (~ 0.4 eV energy spread), 0.15 nm spot size[25], and a beam current of 70-100 pA.

We did our exposures by imaging the resist with a Digiscan Control Unit, embedded within the Digital Micrograph Suite (Gatan, Inc.) choosing: (1) the desired dwell time; (2) microscope magnification; (3) number of pixels; and (4) beam current. These parameters define the area and pitch of interest. No pattern generator was used.

8.3. TEM metrology

The TEM metrology was done on a JEOL JEM 2010F transmission electron microscope at 200 keV. A standard <011> Si sample was used to calibrate the magnification for the TEM camera. The images were taken slightly defocused in order to provide a slight Fresnel fringe to enhance edge contrast. This has a small to negligible effect on the measured resolution.

8.4. Lithographic PSF: dot-exposure method

Isolated posts were patterned with single-pixel exposures with doses ranging from 1 to 10^3fC/dot, followed by salty development[24]. The reciprocal dot dose was then plotted versus the dot radius, as described in Ref. [26], given the functional form of the point-spread function (PSF). We minimized the effect of resist development in the PSF measurement by choosing a developer (salty development[24]) with high contrast, which reduces the uncertainty of the dot-radius measurement (a detailed discussion can be found on a previous report[23]). The standard deviation for the radii of the PSF data sets (Figure 4b-c of the main text) was 0.3 nm.

9. Lithographic point-spread function and its components

The classical formulation of the lithographic PSF is a convolution of the direct-beam PSF and the SE PSF.[13, 14, 26, 27]

$$PSF_{(r)}^{litho} = PSF_{(r)}^{direct-beam} * PSF_{(r)}^{SE} \tag{13}$$

This formulation was conceived assuming that high-energy SEs are the particles responsible for delocalization of deposited energy in the resist.

Here we assumed that delocalization of deposited energy in the resist was caused by SEs, created by direct ionization of valence and core electrons ($PSF_{(r)}^{direct-SE}$), and by VPs, which may also decay into SEs. The total effect from VPs and SEs originated from VPs is $PSF_{(r)}^{VP-SE}$:

$$PSF_{(r)}^{VP-SE} = PSF_{(r)}^{VP} * PSF_{(r)}^{VP-SE\ decay} \tag{14}$$

where $PSF_{(r)}^{VP}$ is given in Figure 3d and provides the energy-density deposited by VPs. $PSF_{(r)}^{VP-SE\ decay}$ provides the energy deposition caused by SEs that originated from VPs. The $PSF_{(r)}^{VP-SE\ decay}$ may not be necessary because we have not defined whether VPs directly expose the resist or whether SEs emitted from VPs expose the resist. Either way, this $PSF_{(r)}^{VP-SE\ decay}$ has negligible spatial effect because these SEs have small energies (<50 eV), and therefore have a small maximum range (<1nm). For simplicity, we excluded the $PSF_{(r)}^{VP-SE\ decay}$

We assumed that an energy-loss event from 10 to 50 eV is due to VP excitation, and an energy-loss event from 50 to 1000 eV is due to SE generation. This division is a good approximation due to the relative cross sections of VPs and SEs in these respective energy ranges. We acknowledge that there are cascading possibilities following these primary excitations, such as excited VPs generating SEs. In addition, the excited SEs may generate VPs and other SEs. Therefore, this is a first order approximation of the effect of SEs relative to VPs. Furthermore, we note that this approximation defines an upper limit of energy loss due to SEs and VPs because a small fraction of energy loss events at 200 keV may not directly generate a SE or VP.[8, 28]

According to the energy division above, the lithographic PSF may be written as:

$$PSF_{(r)}^{litho} \cong a \times PSF_{(r)}^{direct-beam\ E>50\ eV} * PSF_{(r)}^{direct-SE} + b \times PSF_{(r)}^{direct-beam\ E<50\ eV} * PSF_{(r)}^{VP} \quad (15)$$

According to the nomenclature in Figure 4c, we can write formula (14) as:

$$PSF_{(r)}^{litho} \cong total - energy - density_{(r)} \cong\ a \times energy - density_{(r)}^{SEs} + b \times\ energy - density_{(r)}^{VPs} \quad (16)$$

where a= 65% and b=35%, which are the percentages of measured energy loss for SEs (50<Ɛ<1000 eV) and VPs (10<Ɛ<50 eV) respectively (see Figure S3). Formula (16) was normalized by setting the spatial integration of $PSF_{(r)}^{litho}$ to unity. $energy - density_{(r)}^{SEs}$ was simulated by the Monte Carlo model described in section 7 and it was convolved with the instrument spot size. An alternative calculation would be to convolve the direct-beam PSF for energies higher than 50 eV to the SE PSF. We chose not to do this alternative calculation because the direct-beam PSF was not measured up to 1000 eV. $energy - density_{(r)}^{VPs}$ was calculated by a convolution between the direct-beam PSF for energies smaller than 50 eV and the VP PSF.

Considering that the direct-beam PSF does not change significantly between the measured range from 5 to 120 eV, we may approximate the lithographic PSF to:

$$PSF_{(r)}^{litho} \approx PSF_{(r)}^{direct-beam} * (aPSF_{(r)}^{direct-SE} + bPSF_{(r)}^{VP}) \quad (17)$$

10. References

1. Egerton, R. F. *Reports on Progress in Physics* 2009, 72, 016502.
2. Egerton, R. F., *Electron Energy-Loss Spectroscopy In The Electron Microscope*. Third Ed.; Springer New York Dordrecht Heidelberg London: 1986.
3. Silvis-Cividjian, N.; Hagen, C.; Kruit, P. *Journal of Applied Physics* 2005, 98, 084905.

4. Gonze, X.; Rignanese, G.; Verstraete, M.; Beuken, J.; Pouillon, Y.; Caracas, R.; Jollet, F.; Torrent, M.; Zerah, G.; Mikami, M.; Ghosez, P.; Veithen, M.; Raty, J.; Olevano, V.; Bruneval, F.; Reining, L.; Godby, R.; Onida, G.; Hamann, D.; Allan, D. *Zeitschrift Fur Kristallographie* 2005, 220, 558-562.
5. Ritchie, R.; Hamm, R.; Turner, J.; Wright, H.; Ashley, J.; Basbas, G. *Nuclear Tracks And Radiation Measurements* 1989, 16, 141-155.
6. Wolff, P. *Physical Review* 1953, 92, 18-23.
7. Hamm, R.; Turner, J.; Ritchie, R.; Wright, H. *Radiation Research* 1985, 104, S20-S26.
8. Udalagama, C.; Bettiol, A.; Watt, F. *Physical Review B* 2009, 80, 224107.
9. Gonze, X.; Amadon, B.; Anglade, P.; Beuken, J.; Bottin, F.; Boulanger, P.; Bruneval, F.; Caliste, D.; Caracas, R.; Cote, M.; Deutsch, T.; Genovese, L.; Ghosez, P.; Giantomassi, M.; Goedecker, S.; Hamann, D.; Hermet, P.; Jollet, F.; Jomard, G.; Leroux, S.; Mancini, M.; Mazevet, S.; Oliveira, M.; Onida, G.; Pouillon, Y.; Rangel, T.; Rignanese, G.; Sangalli, D.; Shaltaf, R.; Torrent, M.; Verstraete, M.; Zerah, G.; Zwanziger, J. *Computer Physics Communications* 2009, 180, 2582-2615.
10. Heyde, T.; Burgi, H.; Burgy, H.; Tornroos, K. *Chimia* 1991, 45, 38-40.
11. Goedecker, S.; Teter, M.; Hutter, J. *Physical Review B* 1996, 54, 1703-1710.
12. Raghunathan, A.; Hartley, J. *Journal of Vacuum Science & Technology B* 2013, 31, 011605.
13. Wu, B.; Neureuther, A. *Journal of Vacuum Science & Technology B* 2001, 19, 2508-2511.
14. Murata, K.; Kyser, D.; Ting, C. *Journal of Applied Physics* 1981, 52, 4396-4405.
15. Ghanbari, R. A. Physics And Fabrication of Quasi-One-Dimensional Conductors. Ph D, Massachusetts Institute of Technology, 1993.
16. Joy, D.; Luo, S. *Scanning* 1989, 11, 176-180.
17. Hovington, P.; Drouin, D.; Gauvin, R.; Joy, D.; Evans, N. *Scanning* 1997, 19, 29-35.
18. Drouin, D.; Hovington, P.; Gauvin, R. *Scanning* 1997, 19, 20-28.
19. Luo, S.; Joy, D. *Scanning Microscopy* 1990, 127-146.
20. Duan, H.; Manfrinato, V.; Yang, J.; Winston, D.; Cord, B.; Berggren, K. *Journal of Vacuum Science & Technology B* 2010, 28, C6H11-C6H17.
21. Duan, H.; Winston, D.; Yang, J.; Cord, B.; Manfrinato, V.; Berggren, K. *Journal of Vacuum Science & Technology B* 2010, 28, C6C58-C6C62.
22. Manfrinato, V.; Cheong, L.; Duan, H.; Winston, D.; Smith, H.; Berggren, K. *Microelectronic Engineering* 2011, 88, 3070-3074.
23. Manfrinato, V.; Zhang, L.; Su, D.; Duan, H.; Hobbs, R.; Stach, E.; Berggren, K. *Nano Letters* 2013, 13, 1555-1558.
24. Yang, J.; Berggren, K. *Journal of Vacuum Science & Technology B* 2007, 25, 2025-2029.
25. Zhu, Y.; Inada, H.; Nakamura, K.; Wall, J. *Nature Materials* 2009, 8, 808-812.
26. Rishton, S.; Kern, D. *Journal of Vacuum Science & Technology B* 1987, 5, 135-141.
27. Kyser, D.; Viswanathan, N. *Journal of Vacuum Science & Technology* 1975, 12, 1305-1308.
28. Cullen, D.; Perkins, S.; And Seltzer, S., Tables And Graphs of Electron Interaction Cross Sections From 10 Ev To 100 Gev Derived From The LLNL Evaluated Electron Data Library (EEDL), Z = 1 - 100,. Lawrence Livermore National Laboratory, UCRL-50400: 1991; Vol. 31.